

THESIS

SILICON DIOXIDE PLANARIZATION:  
IMPACTS ON OPTICAL COATINGS FOR HIGH ENERGY LASERS

Submitted by:

Travis E. Day

Department of Electrical and Computer Engineering

In partial fulfillment of the requirements

For the Degree of Master of Science

Colorado State University

Fort Collins, Colorado

Fall 2017

Master's Committee:

Advisor: Carmen Menoni

Mario Marconi

John Williams

Copyright by Travis Day 2017

All Rights Reserved

## ABSTRACT

### SILICON DIOXIDE PLANARIZATION: IMPACTS ON OPTICAL COATINGS FOR HIGH ENERGY LASERS

The work of this thesis is devoted to examining the impact of silicon dioxide (silica or SiO<sub>2</sub>) planarization on the optical properties and laser damage resistance of thin-film coatings. SiO<sub>2</sub> planarization is a process to smooth out fluence limiting nodular defects within multilayer coatings for high-energy laser applications. Mitigating these defects will improve the power handling abilities and improve the lifetime of laser coatings.

Presented here is a combination of work with the aim of evaluating the optical and laser damage properties of SiO<sub>2</sub> planarization within single layers, bilayers, and multilayers. As compared to control (non-planarized) samples, a 2-3x increase in the thin-film absorption, which decreases with post-process annealing, was discovered for SiO<sub>2</sub> planarized samples. This suggests that planarization creates oxygen-related defects which can be annealed out and little impurity implantation. Investigations of laser damage resistance were carried out at  $\lambda = 1030\text{nm}$  and pulse durations of  $\tau = 220\text{ps}$  and  $9\text{ps}$ . The laser damage of single and bilayer coatings is known to be dependent on the substrate-coating interface and this is further evidenced within this thesis. This is because the effects of planarization are masked by the extrinsic laser damage processes within the single and bilayers. Slight change (<15%) in the laser induced damage threshold (LIDT) at 220ps and 9ps was observed for planarized single and bilayers. Depending on coating design, post-process annealing was shown to increase the LIDT by ~10% to ~75% at 220ps and ~10% to ~45% at 9ps. Although the fused silica substrate surface LIDT was shown to follow the  $\sqrt{\tau}$  pulse scaling law for pulses above ~10ps, the single and bilayer coatings do not follow this pulse

scaling. The divergence from the  $\sqrt{\tau}$  pulse scaling on the coatings suggests a variation in the laser damage initiation mechanisms between 220ps and 9ps.

Multilayer high-reflecting (HR) mirrors with varying planarization design were also damage tested. A 6-7 J/cm<sup>2</sup> LIDT, with 220ps, was observed for HR coatings with SiO<sub>2</sub> planarization layers within high electric-field areas within the coating. However, SiO<sub>2</sub> planarization at the substrate-coating interface, where the electric-field is minimal, and control (non-planarized) was shown to have a LIDT of  $63 \pm 1.2$  J/cm<sup>2</sup> and  $21.5 \pm 0.5$  J/cm<sup>2</sup> for 220ps, respectively. At 9ps, the LIDT varied less than 90% difference between the various planarization designs. The substrate-coating planarization multilayer and control coating had an equal LIDT of  $9.6 \pm .3$  J/cm<sup>2</sup> at 9ps.

## ACKNOWLEDGEMENTS

This work is supported and performed under the auspices of the U.S. Department of Energy by Lawrence Livermore National Laboratory under contract DE-AC52-07NA27344. I would like to thank Christopher Stolz at Lawrence Livermore National Laboratory (LLNL) for his guidance, aid, and support with laser damage tests and discussions about planarization processing. I am also grateful for the discussions of the results and collaboration with the laser damage research team at LLNL.

My gratitude goes out to many of my friends and colleagues who have aided me: Dr. Elzbieta Jankowska, Dr. Brendan Reagan, HanChen Wang, Fabio Cavalcante, Le Yang, and Emmett Randel. I recognize my graduate advisor Dr. Carmen Menoni for her guidance and unyielding perseverance during my graduate career. Dr. Mario Marconi and Dr. John Williams were especially helpful – my appreciation goes out to them.

I am indebted to my parents, Dr. Bob Day and Reta Day, and family for fostering scientific adventures throughout my childhood and helping me become the best version of myself. Also, though they may not understand how much love they have given, I am grateful for my two cats (Agis and Marley) and two dogs (Baxter and Roxane) for always lifting my spirit. I would especially like to recognize my better-half, Connor Jordan, for his loving support and patience – he is my horizon on the turbulent sea.

## TABLE OF CONTENTS

ABSTRACT .....	ii
ACKNOWLEDGEMENTS .....	iv
1.0 CHAPTER 1: INTRODUCTION .....	1
1.1 NIF LASER AND MATERIAL ISSUES .....	2
1.2 DEFECTS IN MULTILAYER COATINGS AND LASER DAMAGE ISSUES .....	5
1.3 PLANARIZATION OF THIN FILM COATINGS .....	8
1.4 MOTIVATION AND INVESTIGATIONS OF THIS THESIS .....	11
REFERENCES .....	13
2.0 CHAPTER 2: EXPERIMENTAL DETAILS .....	18
2.1 SAMPLES FOR EXPERIMENT .....	18
2.2 ION BEAM SPUTTERING DEPOSITION .....	20
2.3 PLANARIZATION CONDITIONS .....	22
2.4 CHARACTERIZATION METHODS .....	23
2.4.1 PHOTOTHERMAL COMMON-PATH INTERFEROMETRY (PCI) .....	24
2.4.2 X-RAY ANALYSIS .....	25
2.4.2.1 X-RAY PHOTOELECTION SPECTROSCOPY (XPS) .....	25
2.4.2.2 ENERGY DISPERSIVE X-RAY SPECTROSCOPY (EDS) .....	26
2.4.3 THIN-FILM STRESS FROM CARRIER FREQUENCY INTERFEROMETRY (CIF) .....	27
2.4.4 LASER INDUCED DAMAGE THRESHOLD (LIDT) .....	29
REFERENCES .....	36
3.0 CHAPTER 3: IMPACTS OF SiO <sub>2</sub> PLANARIZATION ON OPTICAL THIN-FILM PROPERTIES AND LASER DAMAGE RESISTANCE .....	38
3.1 INTRODUCTION .....	38
3.2 EXPERIMENT .....	39
3.3 RESULTS .....	42
3.4 CONCLUSION .....	47
REFERENCES .....	49
4.0 CHAPTER 4: THIN-FILM PLANARIZATION OF SINGLE AND MULTILAYERS AT PULSE DURATIONS OF 9PS AND 220PS .....	51
4.1 INTRODUCTION .....	51
4.2 EXPERIMENTAL METHODS .....	52
4.2.1 COATING DESIGNS AND DEPOSITION METHODS .....	52
4.2.2 CHARACTERIZATION METHODS .....	53
4.3 RESULTS .....	55
4.3.1 SINGLE AND BILAYER LASER DAMAGE .....	55
4.3.2 MULTILAYER LASER DAMAGE .....	60
4.4 DISCUSSION AND CONCLUSION .....	63
REFERENCES .....	65
5.0 CHAPTER 5: CONCLUSION AND FUTURE WORK .....	67

## CHAPTER 1

### INTRODUCTION

The purpose of this chapter is to review the background of the project and current status of the research in laser damage of optical coatings, coating requirements for fusion lasers, planarization processing of thin films, and the motivation of this work.

Theodore Maiman, on May 21, 1960, first demonstrated light amplification by stimulated emission of radiation (laser) within a ruby rod [1] – thus the laser was born. This ruby laser consisted of a ruby rod resonator with silver coatings on either end which was housed within a metal sleeve and pumped with a helium flash lamp. After the first laser demonstration, laser induced damage (LID) research quickly followed. Within a year of the first ruby laser demonstration, some researchers reported a complication and difficulty of laser operation due the “output light burned holes in the silvered surfaces” on the laser rods [2]. In the early days, laser damage originated from inclusions and impurities within the laser rod material thus limiting the capacity for higher throughput. Over time, the research in laser damage has shifted from the bulk optics to the thin-film coating surfaces which are used for controlling reflection and transmission in laser cavities and optical systems [3]. During the previous five decades, a great deal of research has improved the power handling capability of laser optics by many times. As the research matured, LID solutions remain elusive in part due to the large parameter space in which lasers operate – from pulse durations ranging over 18 orders of magnitude and wavelengths spanning the deep infrared to x-rays [3,4]. LID may generally fall within two mechanism categories: extrinsic mechanisms associated with absorbing inclusions and various defects within the coating and intrinsic mechanisms associated with inherent processes natural to a nascent material [3-6]. Furthermore, there is a clear dependence on pulse duration, wavelength, beam diameter, repetition rate, deposition processes, materials, substrate finish, surface roughness, etc [3-7]. For

example, in the short pulse regime (<10ps) multiphoton ionization, avalanche ionization, and other nonlinear processes dominate LID, whereas within the long pulse regime (>20ps) linear optical absorption and contaminating materials and defects dominate [3,5,6].

Throughout the development of laser technology LID has played both a negative role (limiting the laser output power) and positive role (providing a material processing tool). For these reasons, the field of research into understanding the basic mechanisms of laser damage and improving the laser induced damage threshold (LIDT) on coatings are essential. First held in 1969, the SPIE laser damage conference is solely dedicated to laser induced damage research [7].

## 1.1 NIF LASER AND MATERIAL ISSUES

Soon after the first laser demonstration it was predicted that the laser, with its high energy density, had the capability to generate the basic conditions to realize fusion ignition – thus inertial confinement fusion (IFC) was formed [8,9]. The fusion laser at National Ignition Facility (NIF) in Lawrence Livermore National Laboratory (LLNL) is the largest laser system ever developed [9-12]. NIF is a 70,000m<sup>2</sup> facility housing 192 beam lines which can deliver 1.8MJ of 351nm light [9,10]. As displayed in Figure 1, each identical beam line is the originating point of the laser system which contain multiple flashlamp pumped Nd-glass amplifiers (lasing at 1053nm) [10,12].

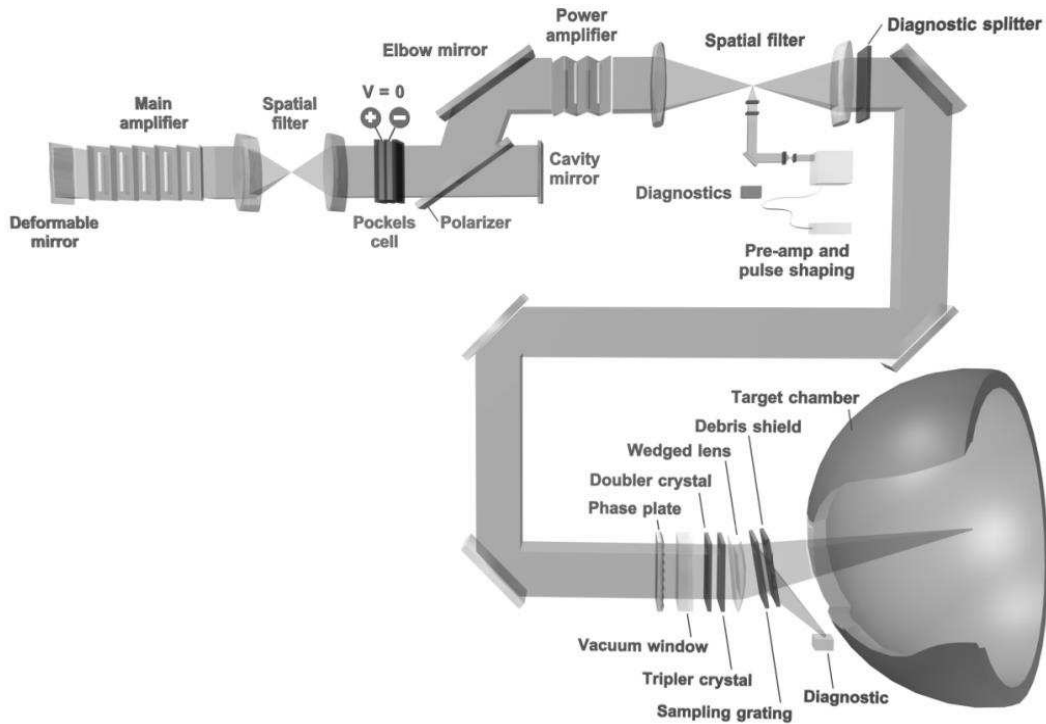


Figure 1: Diagram of one of the 192 beam line trajectories to the target chamber. On the top left is the “laser bay” which holds the main amplifier q-switched cavity. Laser pulses are then route through a second (power) amplifier and spatial frequency filters. This amplified beam is routed through the “switch yard” and into the final optics assembly. After being frequency tripled, the laser is steered into the target chamber to produce nuclear fusion [10].

The multi-pass amplifier is a Q-switched system with two round trips in the laser cavity [10-12]. The laser is then amplified once more through the power amplifier, routed to the target vacuum chamber and frequency tripled before entering the vacuum chamber [10-12]. For the processes of laser fusion, these laser beams are aligned onto a millimeter sized hohlraum comprised of tritium and deuterium [9]. The capsule is energized by the 192 beam lines, producing x-rays, which ablate the target and produce temperatures and pressures equivalent to that of the sun and perform nuclear fusion [9,11].

Due to the high energy requirements of the laser to create fusion the NIF laser uses large-aperture optics (up to one meter in diagonal, as shown in Figure 2) [9,10]. In total, NIF contains over 7,300 large-aperture optics and approximately 30,000 small-aperture optics [9]. Multilayer transition-

metal oxide interference coatings consisting of  $\text{HfO}_2$  and  $\text{SiO}_2$  deposited on BK7 substrates makes up all the high-reflecting mirrors (HR) and beam splitters; anti-reflective (AR) coatings of porous silica and sol-gel coatings are used on the transmissive optics [10-11]. Often fusion lasers are energy and power restricted by the laser induced damage limitations of the optics and coatings applied. In order to improve the lifetime and limit the operational cost in the laser system, LLNL and NIF have devoted a continuous effort to basic science and engineering research to reduce and mitigate laser damage. Since 1997, the number of surface damage sites, particularly on  $3\omega$  optics, has dropped by four orders of magnitude [9-13].

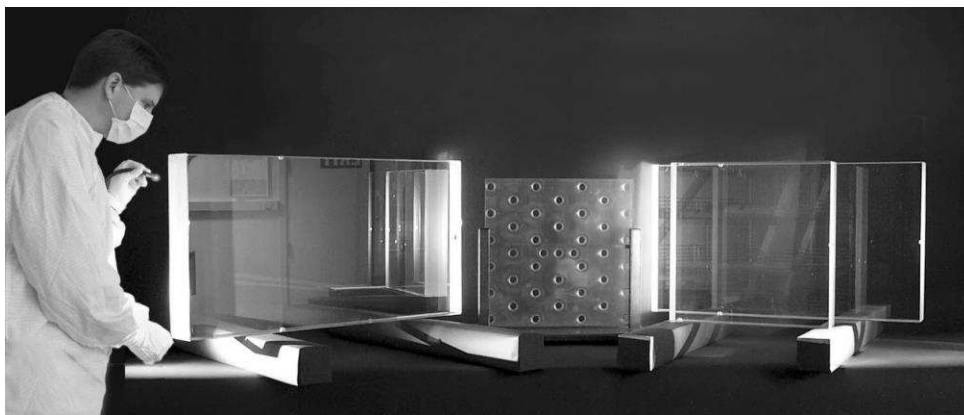


Figure 2: Cavity and polarizer optics being visually inspected before instillation into the laser system [11].

The LID research effort can be characterized within three basic material groups: bulk optical materials, polished optics, and optical coatings [9-11]. Primarily in bulk optics, KDP and fused silica laser glasses are of particular interest. Research has progressed to manufacture bulk laser glass free of inclusions [14] and laser or thermal annealing can greatly increase the LIDT [14-17]. For optical surfaces, the subsurface defects introduced through the polishing process are of primary interest [10,18]. At  $3\omega$ , these defects can be mitigated through laser conditioning [19] or post-polish etching [20,21]. Laser damage reduction and mitigation of multilayer interference coatings is of intense research concentration and is of particular interest to this thesis. As with other materials,  $\text{HfO}_2$  and  $\text{SiO}_2$  multilayer mirrors are also laser conditioned to increase their damage resistance to up to 2-3x

unconditioned values [22,23]. The following section is dedicated to reviewing the role of defect initiated damage in multilayer coatings and mitigation processes such as laser conditioning and planarization.

## 1.2 DEFECTS IN MULTILAYER COATINGS AND LASER DAMAGE ISSUES

Laser induced damage in a dielectric transition-metal oxide multilayer coating is often characterized as a local phenomenon. This damage is often initiated by a random distribution of defects within the coating or at the coating substrate surface. The word “defect” is often used as a general term to refer to a large diversity of extrinsic imperfections within the coating. Defects can vary in both size (from nano-sized to micron-size) and type (such as: point, interband, interstitial, vacancy defects, etc. or larger impurities such as: dust, debris, coating flakes, substrate nodules, etc.) [3-6,24,25]. Thus, the distribution and density of these defects leads to the probabilistic and statistical damage within coatings. While most LIDT tests follow the ISO standard [25], others in the community have developed new statistical measurements that incorporate the defect distribution and probabilities within the laser damage test [26-31]. In particular, NIF employs LID testing using raster scanning for optics with large-areas [30,31].

For large aperture optics used at NIF, nodule defects are of interest. This is in part because nodules tend to be the lowest fluence defects within multilayer coatings and these defects, when damaged, tend to grow with successive pulses [33,34]. The exact nature of nodule seed is not completely known, however it is generally thought they are created from poor substrate surface quality, substrate scratches, leftover polishing slurry, chamber coating flakes, spitting of sputtering source in electron-beam deposition systems, etc. [32-36]. Indeed nodular defect geometries and densities have been shown to be dependent of deposition conditions and cleaning techniques [32,34,35]. When these seeds become covered with successive layers of coating material to form a laser mirror they create a domed nodule on the top surface layer and parabolic cross-section. This is shown schematically in Figure 3. This simplistic model shows that the nodule diameter is given by:  $D = \sqrt{(C \cdot d \cdot T)}$ , where C is a thin

film deposition specific constant,  $d$  is the seed diameter, and  $T$  is the seed depth in the coating [37]. This model generally holds true for real-world coatings [37,38].

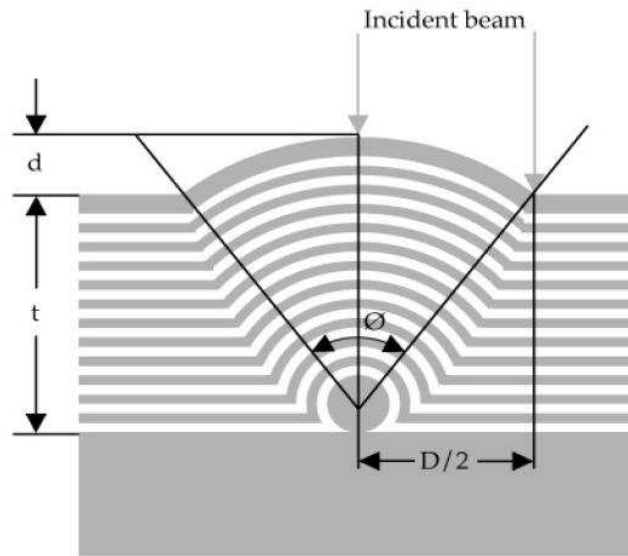


Figure 3: Theoretical model of the geometry of a nodular defect. Image shown is a cross-section of the multilayer coating, with the substrate at the bottom and multilayer coating shown as gray and white layers [39].

Due to the large stresses introduced into the coating, the thermomechanical stability of the nodule seed is extremely poor and there are typically voids near the seed and coating interface. Thus, under intense laser irradiation, a large temperature and stress gradient develops [39,40]. This then leads to the nodule being ejected and damage cratering at the seed boundary. A standing wave electric field (SWEF) is induced into the coating, shown in Figure 4, by the nodule. Research has shown that, depending on the specific nodule geometry, the electric field can be intensified into the coating above and at the nodule seed location [40-45]. Excellent agreement between the damage morphologies and simulated electric-field intensity has been found [40,43]. This SWEF enhancement is what leads to the decrease in the LIDT for coatings with a large density of nodular defects. Under the best deposition and cleaning conditions, these nodules can be significantly reduced. However, they have not been completely reduced for large aperture optics. This limits the total lifetime of the coatings, increases running costs, and restricts the total laser energy.

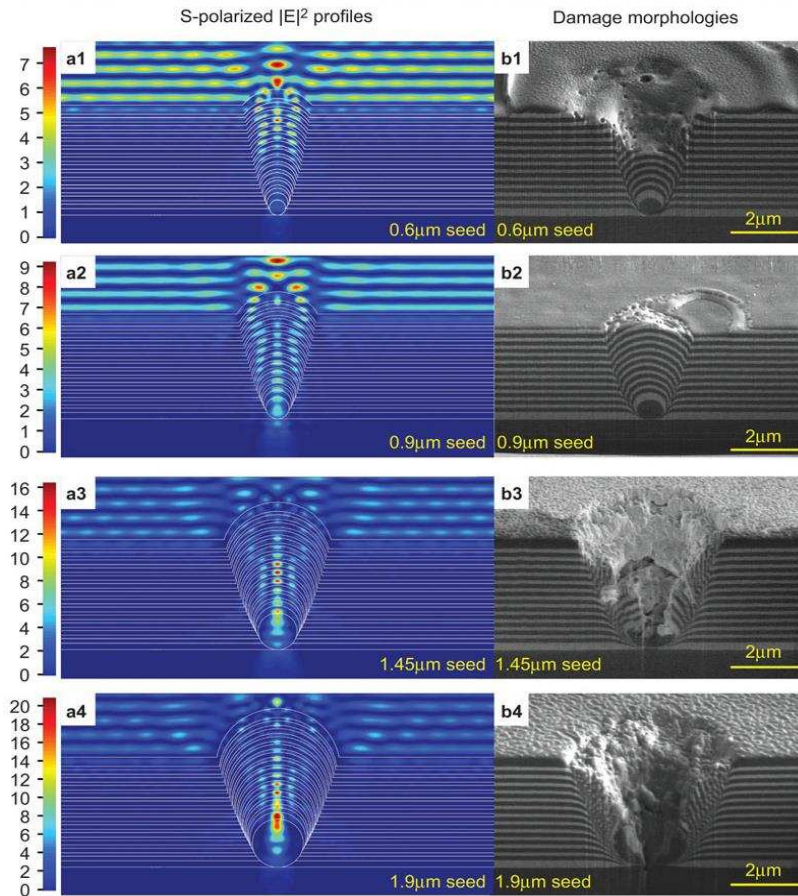


Figure 4: Finite-difference time-domain simulated  $E^2$  distributions (a1-a4) and laser damage morphologies (b1-b4) of nodules. Good agreement between the highest intensity E-field locations and the damage morphology was found [40].

Many mitigation processes were developed with the goal of reducing the limitations of these defects on laser damage or reducing the defect density entirely. In particular, laser conditioning is used on many of the optics installed in the NIF laser [11,13]. Laser conditioning is a process by which the optic surface is irradiated in an overlapping raster-scan method while increasing fluence from low to the highest operating fluence [22]. After a wealth of research, it was found that the conditioning process gently ejects nodular defects within the coating material [21,23,26-28]. By ejecting the nodules at low fluence the surrounding material does not become damaged and does not grow with successive pulses, thus effectively increasing the LIDT of the coating. Another way of mitigating the detrimental effects of nodules within multilayer coatings is to effectively smooth out the coating around the nodule location

and cover up the nodule. This process is called planarization and will be discussed in depth in the next section.

### 1.3 PLANARIZATION OF THIN FILM COATINGS

Surface morphology and microstructure has long been showed to be effected by ion beam bombardment [49,50]. During ion beam etching a number of surface processes are active (atomic recoils, thermally driven surface diffusion, seeding and masking by contaminates, surface dependent preferential sputtering, grain dependent sputtering for crystalline materials, etc.) which tend to roughen or smooth a surface [49,51-54]. In fact, within certain regimes, ion bombardment can either create ultrasmooth surfaces from an otherwise rough surface [55-58] or produce nanostructures through self-organization of the surface [58,59]. Special attention should be made to the difference between direct ion beam smoothing and ion beam planarization. Where direct ion beam smoothing is mediated through relaxation mechanisms, ion beam planarization is a technique mediated through the removal of a sacrificial planarization layer [52]. Ion beam planarization was first developed and shown for semiconductor materials and photoresist [60,61]. It has also been employed in smoothing surfaces for use in the optical spectra [56,62] and multilayer mirrors for use in the extreme ultraviolet (EUV) spectra [63,64].

Ion beam planarization is mediated through two main mechanisms, surface relaxation or surface diffusion and angle dependent etching and sputtering. Smoothing, due to surface diffusion, effectively reduces the slope (from the surface normal) of the highest sloped areas and at high spatial frequencies [65,66]. Thus, the local slopes of the thin film nodule edges are decreased more than the top and surrounding material, resulting in the defect cross-section becoming larger (for example, see Figure 3 and 4). The other mechanism, angular dependent sputter yield or etching rate plays a larger role in planarization. This mechanism drastically reduces the defect cross-section during the etching of the sacrificial planarization layer. This is strictly due to the strong angular dependent etch rate [49,50,67].

The etch rate, shown in Figure 5, increases with incident angle and reaches a maximum around 40°-50° and then decreases for higher angles.

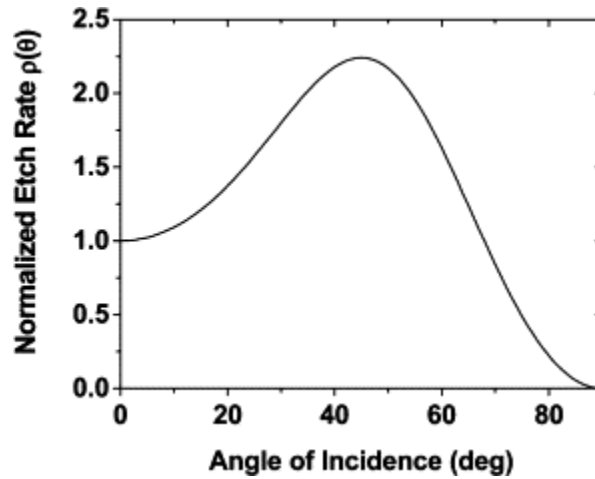


Figure 5: Normalized etch rate is dependent on angle of incidence, from the normal, for an arbitrary material. [67].

The thin film on the edges of the nodule erodes more quickly than the material on the top or surroundings. Thus, the defect profile narrows with successive thin film deposition and etching and collapses with a triangular shaped cross-section. Once the collapse occurs, the defect can be rapidly smoothed and the remaining high-frequency roughness can be minimized by surface relaxation. Altogether, this process is called ion beam planarization.

To apply this process to multilayer interference coatings in the optical regime, one can use  $\text{SiO}_2$  as the sacrificial planarization material. This process involves individually depositing then etching tens-of-nanometers of sacrificial material [68]. These two steps are then repeated until the defect is sufficiently covered.  $\text{HfO}_2$  was also investigated as a planarization material, however likely due to the less angle dependent ion etch rate of the material, it did not planarize as efficiently [69]. Figure 6 shows scanning electron microscope (SEM) images formed with a focused ion beam (FIB) cross-sections. Defects ( $1\mu\text{m}$  tall pillars of varying diameter) were engineered into the substrate through dry-etching [68-70].

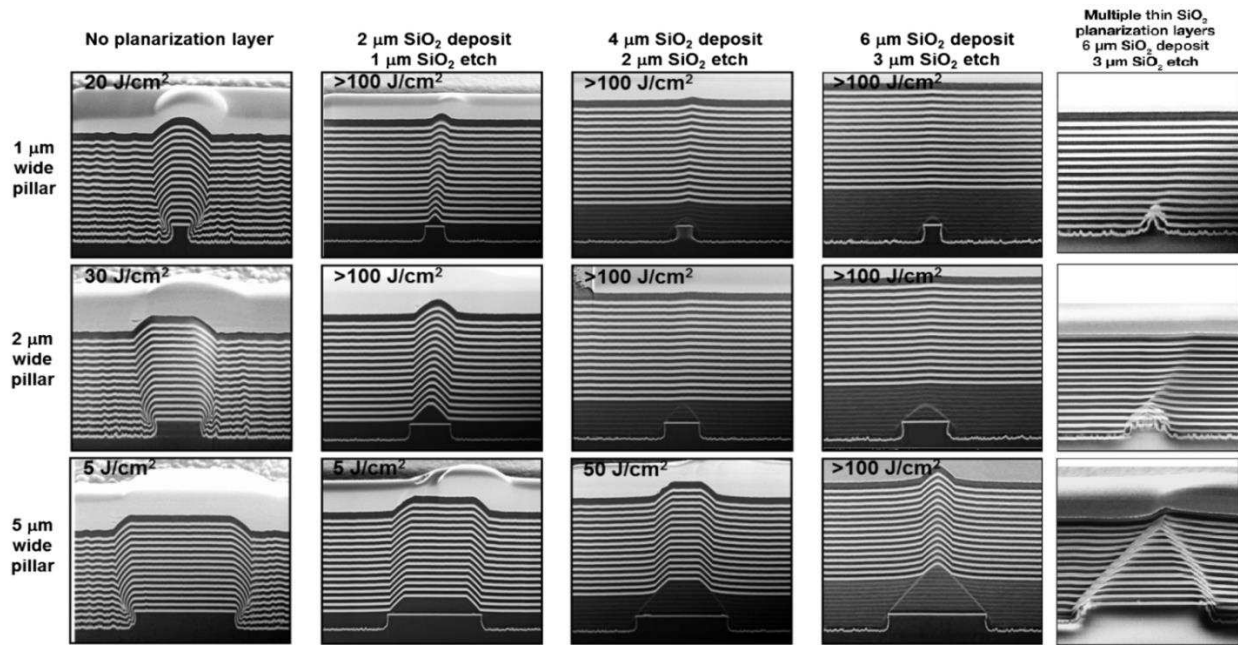


Figure 6: Scanning electron microscope (SEM) images with focused ion beam (FIB) cross-sectional of engineered nodular defects of varying diameter and varying thickness planarization (deposition and etch ratio) and multilayer planarization [70]. Here  $\text{HfO}_2$  layers are white while  $\text{SiO}_2$  layers are black. To observe the surface angle changes, 5nm  $\text{HfO}_2$  layers were added after each planarization cycle.

Thick planarization layers, of varying deposition and etch ratio, were deposited onto the substrate to smooth the defect. For defects of larger diameter, a thicker planarization layer is needed to adequately reduce the nodule cross-section because a wider planarization cone is formed. Employing this process has resulted in a greater than 20x increase in the laser resistance for pulses of 10ns at 1064nm and a 90% reduction in the defect cross-section [69,70]. Multilayer interference coatings were then deposited onto the planarized material. Multilayer planarization, where each  $\text{SiO}_2$  layer within the multilayer interference coating is planarized, was also investigated [71]. Plots for single shot and 600 shot laser damage threshold tests at a wavelength of 1064nm and pulse duration of 10ns for multilayer mirrors as a function of planarization method is shown in Figure 7 [71]. The single shot LIDT for the planarized coatings over 1 $\mu\text{m}$  and 2 $\mu\text{m}$  pillar defects were over 125  $\text{J}/\text{cm}^2$ . Additionally, the LIDT for the multilayer planarization coating is not as high as other planarization designs for 5 $\mu\text{m}$  pillar and 5 $\mu\text{m}$  crater defects. The LIDT for 600 shots per site is nearly half the LIDT for single shot per site, which is

common in multilayer coatings [3,71]. For the non-planarized control coatings, damage only occurred at the engineered defect sites [69].

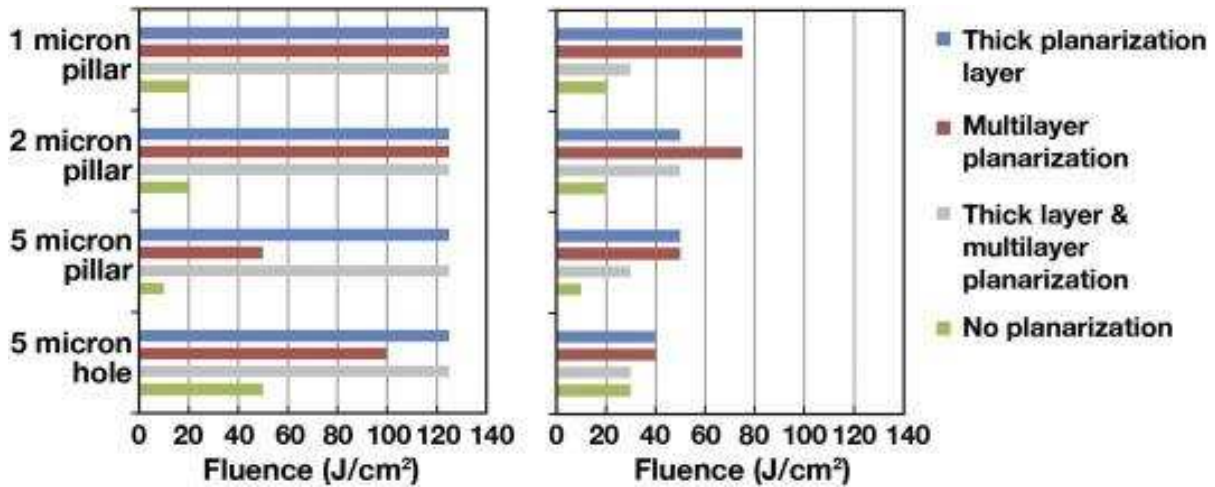


Figure 7: Single shot per site (left) and 600 shots per site (right) laser damage thresholds for wavelength of 1064nm and pulse duration of 10ns for various planarization methods [70].

Planarization within the SiO<sub>2</sub> layers of a multilayer coating has the additional benefit of planarizing any possible nodule defects which seed during the coating process. However, there is a significant limitation which will be discussed within the next section.

#### 1.4 MOTIVATION AND INVESTIGATIONS OF THIS THESIS

It was discovered that multilayer planarization HR coatings had flat-bottomed pit laser damage craters, when tested with 10ns pulses at 1064nm, in all areas of the coating (in non-engineered nodule locations) [70,72]. Additionally, the damage crater depths were found to correspond well with the first top layers of the planarized SiO<sub>2</sub> material within the multilayer [72]. This suggests that planarization induces interfacial defects within the multilayer structure.

It is also well known that high-energy ion beam bombardment of SiO<sub>2</sub> can create point or nano defects (such as E', nonbridging-oxygen hold centers (NBOH), peroxy radicals, neutral oxygen vacancies, etc.) [73-76]. In many cases, these point defects [73-76] have been shown to have detrimental effects on laser damage resistance under a variety of conditions [77-83]. These discoveries lead to a more in-depth

investigation into the impacts of planarization on the optical and micro-structural properties of the thin-film coatings.

The following chapter, chapter 2, will describe the details of the experiment used within this thesis. Of particular importance are the sample designs, ion beam sputtering deposition conditions, planarization methods, and a review of the characterization methods (including thin film absorption, x-ray analysis, (electronic paramagnetic resonance, UV absorption), thin-film stress, and LIDT measurements). Chapter 3 describes the results of optical property and laser damage studies on single and bilayer  $\text{SiO}_2$  (as deposited and planarized) and  $\text{HfO}_2$  films coatings completed with the Yb:YAG laser at 200ps pulse duration. This work was submitted as a conference proceeding at the 2016 SPIE laser damage conference in Boulder, CO (SPIE Proceedings Vol. 10014). Chapter 4 describes further thin-film property and laser damage studies with the Yb:YAG laser at 220ps and 9ps pulse duration. Single and bilayer,  $\text{SiO}_2$  and  $\text{HfO}_2$  films and HR multilayer planarization coatings were investigated. Annealing was correlated with LIDT and absorption for all the coatings. This chapter was submitted as a journal article published. Finally, chapter 6 discusses conclusions of this thesis and future work.

## REFERENCES

1. Maiman, Theodore H. "Stimulated optical radiation in ruby." (1960): 493-494.
2. McClung, F. J., and R. W. Hellwarth. "Giant optical pulsations from ruby." *Applied Optics* 1.101 (1962): 103-105.
3. Wood, Roger M. *Laser-induced damage of optical materials*. CRC Press, 2003.
4. Soileau, M. J. "40 year retrospective of fundamental mechanisms." Boulder Damage Symposium XL Annual Symposium on Optical Materials for High Power Lasers. International Society for Optics and Photonics, 2008.
5. Ristau, Detlev, Marco Jupé, and Kai Starke. "Laser damage thresholds of optical coatings." *Thin Solid Films* 518.5 (2009): 1607-1613.
6. Manenkov, Alexander A. "Fundamental mechanisms of laser-induced damage in optical materials: today's state of understanding and problems." *Optical Engineering* 53.1 (2014): 010901-010901.
7. Proceedings from the annual meetings on "Laser-induced Damage in Optical Materials", 1971 to 2001, available from SPIE.
8. Nuckolls, John, et al. "Laser compression of matter to super-high densities: Thermonuclear (CTR) applications." *Nature* 239.5368 (1972): 139-142.
9. Stolz, Christopher J. "The National Ignition Facility: the path to a carbon-free energy future." *Philosophical Transactions of the Royal Society of London A: Mathematical, Physical and Engineering Sciences* 370.1973 (2012): 4115-4129.
10. Campbell, John H., et al. "NIF optical materials and fabrication technologies: an overview." *Lasers and Applications in Science and Engineering*. International Society for Optics and Photonics, 2004.
11. Stolz, Christopher J., et al. "Fabrication of meter-scale laser resistant mirrors for the National Ignition Facility: a fusion laser." *Optical Science and Technology, SPIE's 48th Annual Meeting*. International Society for Optics and Photonics, 2004.
12. Haynam, C. A., et al. "National Ignition Facility laser performance status." *Applied Optics* 46.16 (2007): 3276-3303.
13. Stolz, Christopher J. "The national ignition facility: the world's largest optical system." *Proc. SPIE*. Vol. 6834. No. 683402. 2007.
14. Campbell, J. H. "Damage resistant optical glasses for high power lasers: A continuing glass science and technology challenge." *GLASS SCIENCE AND TECHNOLOGY-FRANKFURT AM MAIN- 75* (2004): 91-108.
15. Swain, J., et al. "Improving the bulk laser damage resistance of potassium dihydrogen phosphate crystals by pulsed laser irradiation." *Applied Physics Letters* 40.4 (1982): 350-352.
16. Atherton, L. Jeffrey, et al. "Thermal and laser conditioning of production and rapid growth KDP and KD\* P crystals." *Laser-induced damage in optical materials: 1993*. International Society for Optics and Photonics, 1994.
17. Runkel, Michael J., et al. "Results of raster-scan laser conditioning studies on DKDP triplers using Nd:YAG and excimer lasers." *Boulder Damage*. International Society for Optics and Photonics, 2002.

18. Camp, David W., et al. "Subsurface damage and polishing compound affect the 355-nm laser damage threshold of fused silica surfaces." *Laser-Induced Damage in Optical Materials: 1997*. International Society for Optics and Photonics, 1998.
19. Temple, Paul A., W. Howard Lowdermilk, and David Milam. "Carbon dioxide laser polishing of fused silica surfaces for increased laser-damage resistance at 1064 nm." *Applied Optics* 21.18 (1982): 3249-3255.
20. Suratwala, Tayyab I., et al. "HF-based etching processes for improving laser damage resistance of fused silica optical surfaces." *Journal of the American Ceramic Society* 94.2 (2011): 416-428.
21. Brusasco, Raymond M., et al. "UV-laser conditioning for reduction of 351-nm damage initiation in fused silica." *Boulder Damage*. International Society for Optics and Photonics, 2002.
22. Bercegol, Herve. "What is laser conditioning? A review focused on dielectric multilayers." *Proc. SPIE*. Vol. 3578. 1999.
23. Stolz, Christopher J., et al. "Laser conditioning methods of hafnia-silica multilayer mirrors." *Laser-Induced Damage in Optical Materials: 1998*. International Society for Optics and Photonics, 1999.
24. Kozlowski, Mark R., and Robert Chow. "Role of defects in laser damage of multilayer coatings." *Laser-Induced Damage in Optical Materials: 1993*. International Society for Optics and Photonics, 1994.
25. International Organization for Standardization, ISO-21254: Lasers and laser-related equipment- Test methods for laser-induced damage threshold (2011).
26. Bercegol, Herve. "Statistical distribution of laser damage and spatial scaling law for a model with multiple defects cooperation in damage." *Laser-Induced damage in Optical Materials: 1999* 3902 (2000): 339-346.
27. Volto, Patricia, et al. "Refined statistical measurements of laser damage." *Laser-Induced Damage in Optical Materials: 1999*. International Society for Optics and Photonics, 2000.
28. Porteus, J. O., and Steven C. Seitel. "Absolute onset of optical surface damage using distributed defect ensembles." *Applied optics* 23.21 (1984): 3796-3805.
29. Xu, Yeja, Luke A. Emmert, and Wolfgang Rudolph. "Spatio-temporally resolved optical laser induced damage (STEREO LID) technique for material characterization." *Optics express* 23.17 (2015): 21607-21614.
30. Bercegol, Hervé, et al. "The impact of laser damage on the lifetime of optical components in fusion lasers." *XXXV Annual Symposium on Optical Materials for High Power Lasers: Boulder Damage Symposium*. International Society for Optics and Photonics, 2004.
31. Negres, Raluca A., et al. "Apparatus and techniques for measuring laser damage resistance of large-area, multilayer dielectric mirrors for use with high energy, picosecond lasers." *Lasers and Electro-Optics (CLEO), 2015 Conference on*. IEEE, 2015.
32. Cheng, Xinbin, et al. "Laser damage study of nodules in electron-beam-evaporated HfO<sub>2</sub>/SiO<sub>2</sub> high reflectors." *Applied optics* 50.9 (2011): C357-C363.
33. Guenther, Karl H. "Nodular defects in dielectric multilayers and thick single layers." *Applied optics* 20.6 (1981): 1034-1038.
34. Stolz, Christopher J., et al. "Comparison of nodular defect seed geometries from different deposition techniques." *Laser-Induced Damage in Optical Materials: 1995*. International Society for Optics and Photonics, 1996.

35. Chow, Robert, et al. "Reactive evaporation of low-defect density hafnia." *Applied optics* 32.28 (1993): 5567-5574.
36. Qiu, S. Roger, et al. "Impact of substrate surface scratches on the laser damage resistance of multilayer coatings." *Laser Damage Symposium XLII: Annual Symposium on Optical Materials for High Power Lasers*. International Society for Optics and Photonics, 2010.
37. Tench, Robert J., Robert Chow, and Mark R. Kozlowski. "Characterization of defect geometries in multilayer optical coatings." *Journal of Vacuum Science & Technology A: Vacuum, Surfaces, and Films* 12.5 (1994): 2808-2813.
38. Tench, Robert J., Mark R. Kozlowski, and Robert Chow. "Investigation of the microstructure of coatings for high-power lasers by nonoptical techniques." *1994 International Symposium on Optical Interference Coatings*. International Society for Optics and Photonics, 1994.
39. Stolz, Christopher J., Francois Y. Genin, and Thomas V. Pistor. "Electric-field enhancement by nodular defects in multilayer coatings irradiated at normal and 45 incidence." *XXXV Annual Symposium on Optical Materials for High Power Lasers: Boulder Damage Symposium*. International Society for Optics and Photonics, 2004.
40. Cheng, Xinbin, et al. "The effect of an electric field on the thermomechanical damage of nodular defects in dielectric multilayer coatings irradiated by nanosecond laser pulses." *Light: Science & Applications* 2.6 (2013): e80.
41. Genin, Francois Y., and Christopher J. Stolz. "Morphologies of laser-induced damage in hafnia-silica multilayer mirror and polarizer coatings." *Third International Workshop on Laser Beam and Optics Characterization*. International Society for Optics and Photonics, 1996.
42. Kozlowski, M. R., J. F. DeFord, and M. C. Staggs. "Laser-damage susceptibility of nodular defects in dielectric mirror coatings: AFM measurements and electric-field modeling." *AIP Conference Proceedings CONF- 9304144*. Vol. 288. No. 1. AIP, 1993.
43. Staggs, Michael C., et al. "Correlation of damage threshold and surface geometry of nodular defects on HR coatings as determined by in-situ atomic force microscopy." *Optical Materials for High Power Lasers*. International Society for Optics and Photonics, 1993.
44. DeFord, J. F., and Mark R. Kozlowski. "Modeling of electric-field enhancement at nodular defects in dielectric mirror coatings." *Optical Materials for High Power Lasers*. International Society for Optics and Photonics, 1993.
45. Stolz, Christopher J., Michael D. Feit, and Thomas V. Pistor. "Laser intensification by spherical inclusions embedded within multilayer coatings." *Applied optics* 45.7 (2006): 1594-1601.
46. Schildbach, M., Lloyd L. Chase, and Alex V. Hamza. "Investigation of Neutral Atom and Ion Emission During Laser Conditioning of Multilayer HfO<sub>2</sub>-SiO<sub>2</sub> Coatings." *Laser-Induced Damage in Optical Materials: 1990*. ASTM International, 1991.
47. Kozlowski, Mark R., et al. "Laser Conditioning and Electronic Defects of HfO<sub>2</sub> and SiO<sub>2</sub> Thin Films." *Laser-Induced Damage in Optical Materials: 1990*. ASTM International, 1991.
48. Tench, R., et al. "Laser damage and conditioning at defects in optical coatings." *Optical Interference Coatings* 1 (1995): 214.
49. Ohring, Milton. *Materials science of thin films*. Academic press, 2001.
50. Cuomo, Jerome J., Stephen M. Rossnagel, and Harold R. Kaufman. "Handbook of ion beam processing technology." (1989).

51. Harrison, Matt P., and R. Mark Bradley. "Nanoscale patterns formed by ion bombardment of rotating binary materials." *Journal of Physics: Condensed Matter* 27.29 (2015): 295301.
52. Frost, F., et al. "Large area smoothing of surfaces by ion bombardment: fundamentals and applications." *Journal of Physics: Condensed Matter* 21.22 (2009): 224026.
53. Stillwagon, L. E., and R. G. Larson. "Fundamentals of topographic substrate leveling." *Journal of Applied Physics* 63.11 (1988): 5251-5258.
54. de Assis, T. A., and FDA Aarão Reis. "Smoothing in thin-film deposition on rough substrates." *Physical Review E* 92.5 (2015): 052405.
55. Spiller, Eberhard A., et al. "Smoothing of mirror substrates by thin-film deposition." SPIE's International Symposium on Optical Science, Engineering, and Instrumentation. International Society for Optics and Photonics, 1999.
56. Frost, F., et al. "Ion beam assisted smoothing of optical surfaces." *Applied Physics A: Materials Science & Processing* 78.5 (2004): 651-654.
57. Frost, F., et al. "Large area smoothing of optical surfaces by low-energy ion beams." *Thin Solid Films* 459.1 (2004): 100-105.
58. Muñoz-García, Javier, et al. "Self-organized nanopatterning of silicon surfaces by ion beam sputtering." *Materials Science and Engineering: R: Reports* 86 (2014): 1-44.
59. Keller, Adrian, and Stefan Facsko. "Ion-induced nanoscale ripple patterns on Si surfaces: theory and experiment." *Materials* 3.10 (2010): 4811-4841.
60. Johnson, L. F., K. A. Ingersoll, and D. Kahng. "Planarization of patterned surfaces by ion beam erosion." *Applied Physics Letters* 40.7 (1982): 636-638.
61. Fechner, R., et al. "Precision Science and Technology for Perfect Surfaces, ed. by Y. Furukawa, Y. Mori, T. Kataoka (The Japan Society for Precision Engineering, Tokyo 1999) p 249.
62. Johnson, Leo F., and K. A. Ingersoll. "Ion polishing with the aid of a planarizing film." *Applied optics* 22.8 (1983): 1165-1167.
63. Mirkarimi, Paul B., et al. "Advancing the ion beam thin film planarization process to mitigate EUVL mask substrate pit defects." 2004 EUVL Symposium. 2004.
64. Mirkarimi, P. B., et al. "Advancing the ion beam thin film planarization process for the smoothing of substrate particles." *Microelectronic engineering* 77.3 (2005): 369-381.
65. Spiller, Eberhard A., et al. "Smoothing of mirror substrates by thin-film deposition." SPIE's International Symposium on Optical Science, Engineering, and Instrumentation. International Society for Optics and Photonics, 1999.
66. Tong, William M., and R. Stanley Williams. "Kinetics of surface growth: phenomenology, scaling, and mechanisms of smoothing and roughening." *Annual Review of Physical Chemistry* 45.1 (1994): 401-438.
67. Stearns, D. G., P. B. Mirkarimi, and E. Spiller. "Localized defects in multilayer coatings." *Thin Solid Films* 446.1 (2004): 37-49.
68. Stolz, Christopher J., et al. "Planarization of optical substrates." U.S. Patent Application No. 14/434,699.
69. Stolz, Christopher J., et al. "High laser-resistant multilayer mirrors by nodular defect planarization [Invited]." *Applied optics* 53.4 (2014): A291-A296.

70. Stolz, Christopher J., et al. "Defect insensitive 100 J/cm<sup>2</sup> multilayer mirror coating process." SPIE Laser Damage. International Society for Optics and Photonics, 2013.
71. Stolz, Christopher J., et al. "Substrate and coating defect planarization strategies for high-laser-fluence multilayer mirrors." *Thin Solid Films* 592 (2015): 216-220.
72. Stolz, Christopher J., et al. "Depth determination of critical fluence-limiting defects within planarized and non-planarized mirror coatings." SPIE Optical Systems Design. International Society for Optics and Photonics, 2015.
73. Griscom, David L. "Optical properties and structure of defects in silica glass." *Journal of the Ceramic Society of Japan* 99.1154 (1991): 923-942.
74. Devine, R. A. B., and A. Golanski. "Creation and annealing kinetics of magnetic oxygen vacancy centers in SiO<sub>2</sub>." *Journal of Applied Physics* 54.7 (1983): 3833-3838.
75. Devine, R. A. B. "Oxygen vacancy creation in SiO<sub>2</sub> through ionization energy deposition." *Applied physics letters* 43.11 (1983): 1056-1058.
76. Arnold, G. W. "Ion-implantation effects in noncrystalline SiO<sub>2</sub>." *IEEE Transactions on Nuclear Science* 20.6 (1973): 220-223.
77. Rudolph, Wolfgang, et al. "Laser damage in dielectric films: What we know and what we don't." SPIE Laser Damage. International Society for Optics and Photonics, 2013.
78. Xu, Yejia, et al. "Comparison of defects responsible for nanosecond laser-induced damage and ablation in common high index optical coatings." *Optical Engineering* 56.1 (2017): 011019-011019.
79. Emmert, Luke A., Mark Mero, and Wolfgang Rudolph. "Modeling the effect of native and laser-induced states on the dielectric breakdown of wide band gap optical materials by multiple subpicosecond laser pulses." *Journal of Applied Physics* 108.4 (2010): 043523.
80. Markosyan, A. S., et al. "Study of spontaneous and induced absorption in amorphous Ta<sub>2</sub>O<sub>5</sub> and SiO<sub>2</sub> dielectric thin films." *Journal of Applied Physics* 113.13 (2013): 133104.
81. Menoni, Carmen S., et al. "Advances in ion beam sputtered Sc<sub>2</sub>O<sub>3</sub> for optical interference coatings." *Proc. SPIE*. Vol. 7842. 2010.
82. Langston, P. F., et al. "Point defects in Sc<sub>2</sub>O<sub>3</sub> thin films by ion beam sputtering." *Applied optics* 53.4 (2014): A276-A280.
83. Langston, Peter F. A study of the influence of process parameter variations on the material properties and laser damage performance of ion beam sputtered Sc<sub>2</sub>O<sub>3</sub> and HfO<sub>2</sub> thin films.

## CHAPTER 2

### EXPERIMENTAL DETAILS

The purpose of this chapter is to review the experimental details of the research. This includes discussing the samples deposited for the experiments, thin-film deposition and planarization conditions, and briefly describe all characterization methods. It is not the specific goal of this thesis to describe the working principles of all the characterization methods in detail. However, special attention will be paid to the LIDT system. The reader is referenced to many books and review articles on the specific systems throughout.

#### 2.1 SAMPLES FOR EXPERIMENT

As discussed within the previous chapter, multilayer planarization produces higher damage density and shallower flat-bottomed damage craters, for 1064nm laser at 10ns pulses. This result suggests that planarization of SiO<sub>2</sub> produces defects which limit the laser damage resistance. To investigate the differences between the typical as deposited (as dep) SiO<sub>2</sub> and the planarized (planz) SiO<sub>2</sub> a set of single, bilayer, and multilayer interference coatings were produced. The specifics of the deposition and planarization conditions are described in the following sections. All the films were deposited upon UV-grade super polished fused silica substrates purchased from Blue Ridge Optics. The single and bilayer designs, shown in Figure 8, are as follows:

**AsDep** – [Sub]/[2L]; [Sub]/[2L/H]; [Sub]/[H/2L]; and [Sub]/[H]

**Planz** – [Sub]/[2L\*]; [Sub]/[2L\*/H]; and [Sub]/[H/2L\*]

Where L =  $\lambda/4$  (~175nm) SiO<sub>2</sub> as dep, H =  $\lambda/4$  (~125nm) HfO<sub>2</sub> at  $\lambda = 1030\text{nm}$ , \* = full  $\lambda/4$  SiO<sub>2</sub> planarized, and \*\* = first half or bottom half of  $\lambda/4$  of SiO<sub>2</sub> planarized.

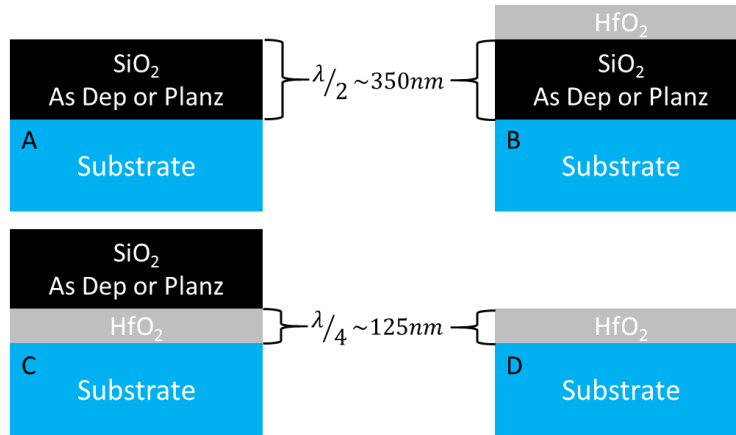


Figure 8: Schematic of single and bilayer coatings grown. (A) is a single layer of  $\text{SiO}_2$  as dep or planz, (B) is a bilayer with  $\text{HfO}_2$  on top of  $\text{SiO}_2$ , (C) is a bilayer with  $\text{SiO}_2$  on top of  $\text{HfO}_2$ , and (D) is a single layer of  $\text{HfO}_2$

Multilayer interference coatings (IC) of various planarization designs were also investigated. Three different multilayer planarization designs and one control (non-planarized) multilayer coating were deposited. The designs are as follows:

$$\text{Planz A} - [\text{Sub}]/[\text{H}/\text{L}^*]^8 / [\text{H}/\text{L}^{**}]^6 / [\text{H}/\text{L}] \text{L}$$

$$\text{Planz B} - [\text{Sub}]/[\text{H}/\text{L}^*]^8 / [\text{H}/\text{L}^{**}]^6 / [\text{H}/\text{L}] \text{L}^*$$

$$\text{Planz C} - [\text{Sub}]/[2\text{L}^*]/[\text{H}/\text{L}]^{15} \text{L}$$

$$\text{Control} - [\text{Sub}]/[\text{H}/\text{L}]^{15} \text{L}$$

Where  $\text{L} = \lambda/4$  ( $\sim 175\text{nm}$ )  $\text{SiO}_2$  as dep,  $\text{H} = \lambda/4$  ( $\sim 125\text{nm}$ )  $\text{HfO}_2$  at  $\lambda = 1030\text{nm}$ ,  $*$  = full  $\lambda/4$   $\text{SiO}_2$  planarized, and  $**$  = first half or bottom half of  $\lambda/4$  of  $\text{SiO}_2$  planarized.

Two samples from each set of coatings were annealed, one at  $300^\circ\text{C}$  for 8 hours and one at  $300^\circ\text{C}$  for 16 hours, in air at atmospheric pressure. The rise and fall time was set to  $1^\circ\text{C}/\text{min}$ . A Horiba ellipsometer was used to measure the thickness of the coatings to insure the deposition process was correct and detect any changes in film thickness with annealing.

Due to the  $\lambda/4$  and  $\lambda/2$  thickness of the sample, a standing wave electric field (E-field) is produced within the coating. This E-field is a function of sample thickness, wavelength, index of

refraction, and angle of incidence [1]. In Figure 9 below, the E-field is calculated using Essential Macleod [2] for sample thicknesses discussed above, wavelength of 1030nm, and normal (0°) angle of incidence.

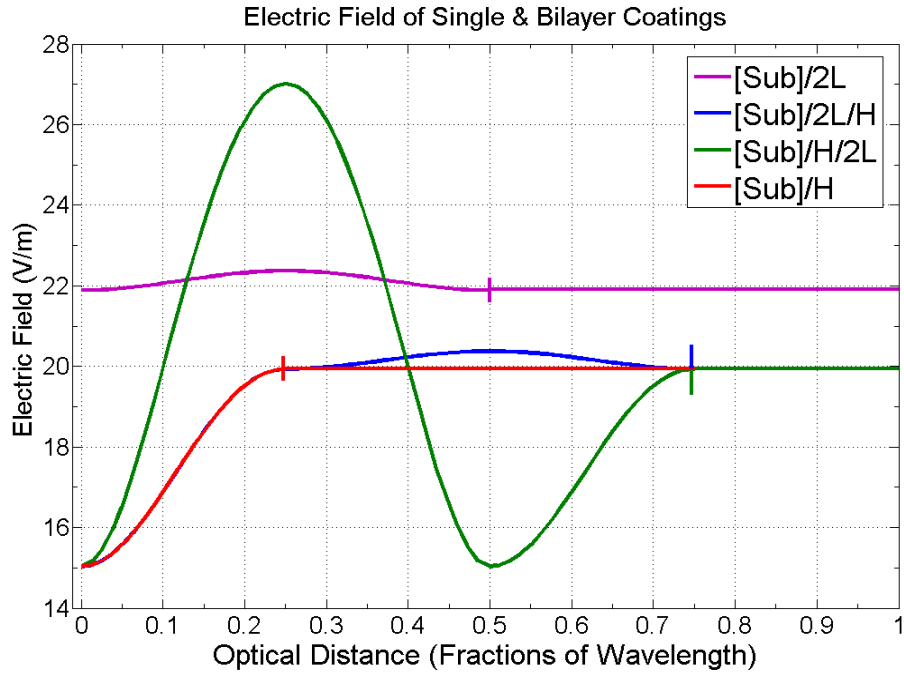


Figure 9: Calculated electric field within the single and bilayer coatings for 1030nm and 0°. The air-film interface is labeled as zero optical distances (y-axis intercept) and the vertical tick marks indicate the coating-substrate interface for each respective coating design.

## 2.2 ION BEAM SPUTTERING DEPOSITION

The details about ion beam sputtering (IBS) deposition have been investigated and explained in depth elsewhere [3-5], therefore this section will not go into great detail. The specific deposition conditions for this work will be discussed.

A Veeco Spector® dual ion beam sputtering system, used to deposit the coatings, is shown schematically in Figure 10. The IBS system is fundamentally a vacuum system which employs two plasma or ion sources, a sputtering target, and sample holders. The vacuum chamber has a volume of  $\sim 1\text{m}^3$  and is able to achieve  $< 5.00 \times 10^{-7}\text{Torr}$  base pressure through a CTI-Cryogenics cryogenic vacuum pump.

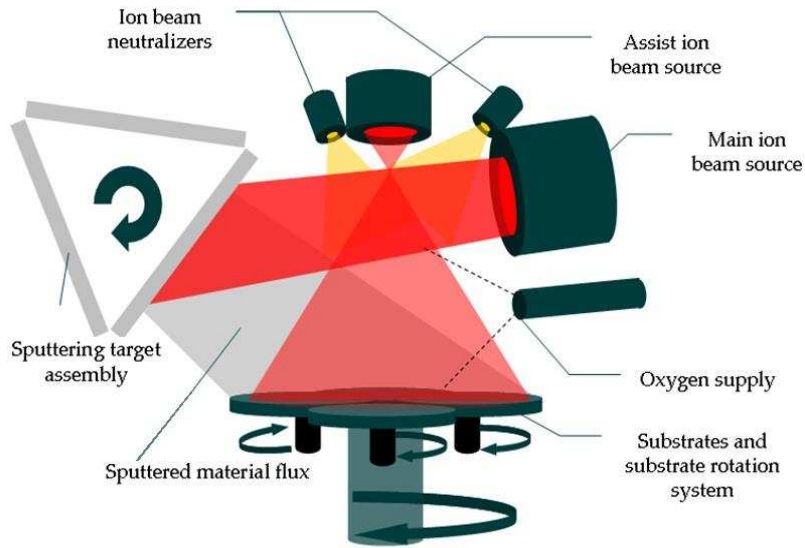


Figure 10: Schematic drawing of the Spector IBS system.

This system uses two radio-frequency (RF) plasma sources. The main, 16cm diameter, sputtering source is responsible for accelerating the ions which then impinge onto the target to sputter material. Both sources use molybdenum grids to accelerate the ions. The sputtering target can be a metal or oxide material. For reactive sputtering of oxide thin-films, molecular oxygen is also introduced into the chamber. These sputtered particles generate a plume of physical-vapor-phase atoms and molecules which condense onto the substrate and produce a thin-film. The secondary source, 12cm diameter, is used for etching, planarization, and altering the optical and micro-structural properties of the film.

It is generally stated that IBS thin-films have good mechanical stability, film density, “bulk-like” refractive index, good uniformity, low losses, and good laser damage resistance, as compared with other deposition techniques. The optical and micro-structural properties of the thin-films produced are dependent on sputtering and deposition conditions. The production of oxygen related defects has been shown to be dependent on oxygen partial pressure and sputtering target material, and are known to exist within these films [5-12]. Additionally, the thin-film properties can be altered by the use of the secondary source during film deposition [13,14] – this is different from planarization processing.

The chosen deposition conditions for this thesis are listed in Table 1 below. In this case, SiO<sub>2</sub> is deposited from a SiO<sub>2</sub> oxide target and HfO<sub>2</sub> is deposited from a Hafnium metallic target. Oxygen was introduced into the chamber at the target surface and with 12sccm flow for both materials.

Table 1: Deposition and etch conditions for thin films grown with IBS.

Ion Source	Source Current	Beam Voltage	Oxygen Flow (sccm)	Deposition/Etch Rate
<b>Deposition Source</b>	600 mA	1250 V	SiO <sub>2</sub> = 12 sccm HfO <sub>2</sub> = 12 sccm	SiO <sub>2</sub> ≈ 2.1 A/s HfO <sub>2</sub> ≈ 1.4 A/s
<b>Assist/Etch Source</b>	150 mA	1000 V	No Oxygen	SiO <sub>2</sub> etch ≈ 0.45 A/s

Before deposition, the system is cleaned and checked for flaking. The substrates are thoroughly cleaned with lint-free lens tissue, acetone, and methanol using the “drop and drag” technique. The substrates are then visually inspected with a fiber-optic light before installing into the vacuum chamber. The system is pumped down to  $\leq 5.00 \times 10^{-7} Torr$ . To achieve this base pressure, the vacuum system is first heated to 100°C for 1 hour to bake out any residual water within the chamber. The chamber is allowed to cool to 60°C before and kept at 60°C during deposition. This temperature is measured by a thermometer probe protruding into the vacuum chamber; this is not the temperature of the substrate, growing film, or sputtering target. Unfortunately, the temperatures of these other surfaces are not completely known.

### 2.3 PLANARIZATION CONDITIONS

The basic theory behind planarization processing was discussed in the previous chapter. Within this section, the exact planarization process and recipe is described.

Unlike previous planarization work, the coatings for this work were not deposited upon substrates with engineered defects [14-16]. A 2:1 deposition to etch ratio was previously found to be optimum; this ratio is used for this work [15]. For planarization processing, 10’s of nano-meters of SiO<sub>2</sub> are deposited then half of this SiO<sub>2</sub> film is etched away. This process is repeated multiple times, in a stepwise fashion, until a desired thickness is reached. This is the essence of planarization processing and

is schematically shown in Figure 11. Typically, a thickness of  $\lambda/4$  (175nm) is reached within 8 planarization cycles.

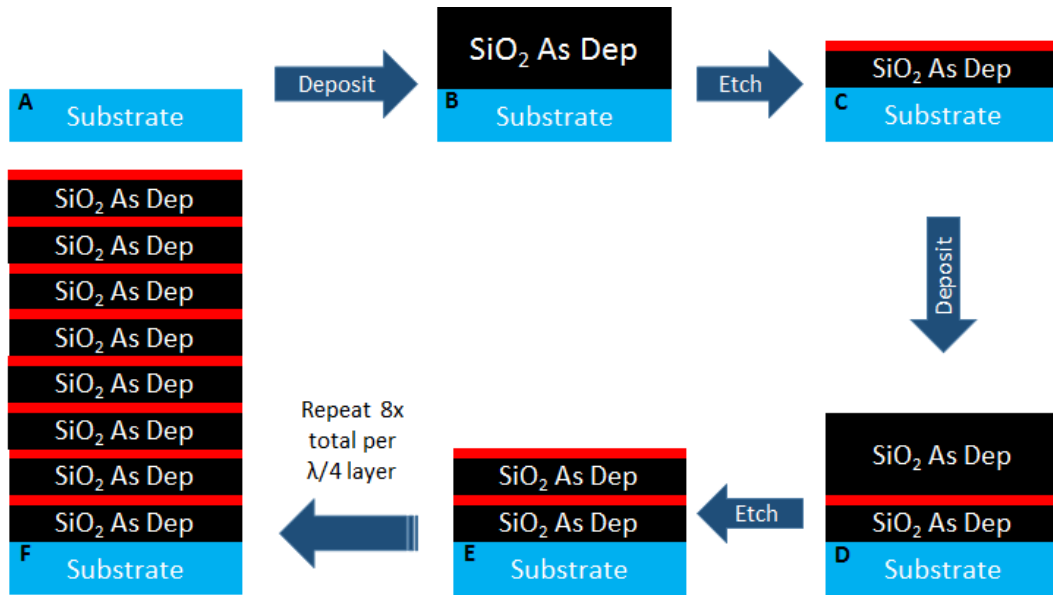


Figure 11: This diagram (not to scale) shows the steps involved in the planarization process. (A) The substrate is cleaned and prepared for deposition, (B) a ~50nm thick SiO<sub>2</sub> layer is deposited, (C) half of the film is then etched away (leaving ~25nm), (D) another ~50nm thick SiO<sub>2</sub> layer is deposited, (E) half of this film is then etched (leaving ~50nm total), (F) this process is repeated until the desired thickness is reached. The thin red bands represent the approximately 3nm penetration depth of Ar ions into the SiO<sub>2</sub> film.

During the etch step, the SiO<sub>2</sub> is bombarded with 1keV Ar<sup>+</sup> ions which were accelerated through molybdenum (Mo) grids. These ions and grid material have the potential to implant into the film and form impurities. Additionally, high energy ion bombardment is known create ion damage within bulk SiO<sub>2</sub> [18-20]. Simple Monte Carlo modeling suggests a 3nm penetration depth under these etch conditions. A short penetration depth produces thin bands throughout the thickness of the coatings where Ar implantations, Mo contamination, and ion created defects may lie. This is shown as red bands in Figure 11.

## 2.4 CHARACTERIZATION METHODS

This section briefly discusses the thin-film material characterization techniques including photothermal common-path interferometry (PCI), X-ray analysis, (electronic paramagnetic resonance (EPR), UV absorption), thin-film stress from carrier frequency interferometry, and laser damage threshold measurements. Many of these characterization and chemistry techniques have been discussed in depth through various books and review papers, thus it is not the goal of this section to describe every method in complete detail.

#### 2.4.1 PHOTOTHERMAL COMMON-PATH INTERFEROMETRY (PCI)

Photothermal Common-path interferometry (PCI) is a very sensitive technique for measuring the optical absorption of a thin-film within the parts-per-million (ppm) range [5,21]. This is a pump and probe technique in which a modulated 1064nm fiber laser (pump) is focused onto the surface thin-film sample. This induces a local heating of the sample and induces a change in the refractive index. This refractive index change is then detected by an unfocused HeNe laser (probe) through self-interference. Finally, this interference can be detected, through the aid of a lock-in amplifier, with a photodiode. An example of the interference is shown in Figure 12. First a calibration sample of known absorption is measured. The absorption of an unknown sample is calculated through maximum voltage recorded on the photodiode and linearly related to the absorption of a calibration sample.

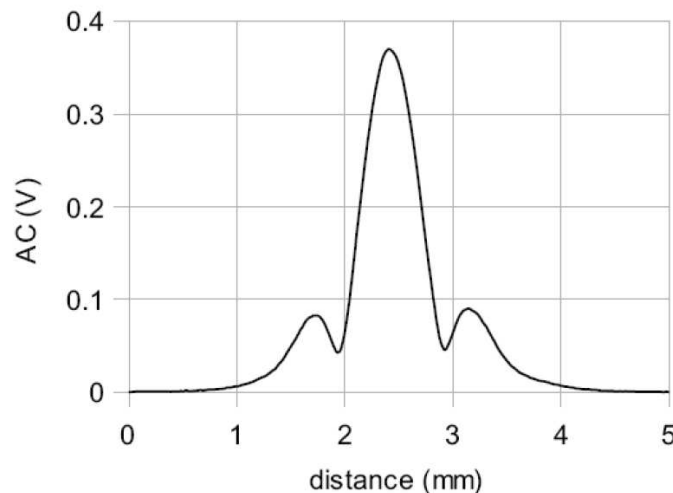


Figure 12: Example of PCI trace for an arbitrary coating made by scanning the coating forward through the pump and probe overlap region [21].

The absorption measurements for this thesis were made using a CSU built PCI. A IPG Photonics fiber amplified Nd:YAG laser operating at 1064nm is focused onto the sample with a focal spot of  $\sim 80\mu\text{m}$  and 2-5W of power. This laser was directly modulated at 400Hz with a Stanford Research Systems model SR810-DSP lock-in amplifier. The sample was positioned normal to the pump laser and scanned with a computer controlled 3-axis stage. After the system was aligned and calibrated, a set of samples was consecutively measured. Each sample was measured at 5-6 total locations and the results averaged.

#### 2.4.2 X-RAY ANALYSIS

Both X-ray photoelectron spectroscopy (XPS) and energy dispersive X-ray spectrometry (EDS) were used in an attempt to detect any changes in the oxygen bonding environment, silicon to oxygen ratios, and impurity implantation of argon and molybdenum. Within this section, the basic principles of XPS and EDS and the operation conditions are discussed.

##### 2.4.2.1 X-RAY PHOTOELECTION SPECTROSCOPY (XPS)

X-ray photoelectron spectroscopy (XPS) is a surface spectroscopic technique which is able to measure the elemental composition in parts-per-thousand (ppt). Of particular importance, XPS can also be used to measure the bonding environment of a molecule. Fundamentally, XPS works upon the photoelectric effect. A spectrum (plot of electron signal intensity versus binding energy) is gathered through irradiating a material with a beam of X-rays while simultaneously measuring the kinetic energy and intensity of electrons which are expelled from the surface (0nm-5nm) [22]. Due to the unique binding energy for each element (corresponding to the electron orbitals), some characteristic spectra can be obtained which is then correlated to identify all elements and elemental percentage within the sample. The working principle is shown in Figure 13. To reduce noise and increase sensitivity, an ultra-high vacuum system is required.

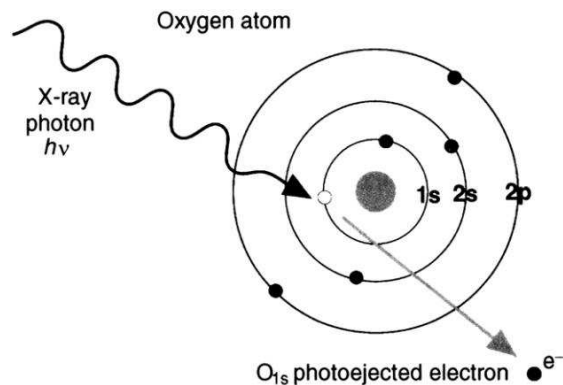


Figure 13: The working principle for XPS is shown for an oxygen atom. An electron from an inner orbital is ejected through photo-excitation with x-rays [22].

The SiO<sub>2</sub> as deposited and planarized films were measured with a high-resolution PE-5800 XPS instrument. This instrument uses Cu K<sub>α</sub> x-rays with a wavelength  $\lambda = 1.5418\text{\AA}$ . Both samples were inserted through a load lock and measured at ultra-high vacuum pressures with a base pressure  $\leq 5.00 \times 10^{-9}\text{Torr}$ . A full spectrum was observed for each sample and high-resolution of the silicon, oxygen, argon, and molybdenum peaks were gathered.

#### 2.4.2.2 ENERGY DISPERSIVE X-RAY SPECTROSCOPY (EDS)

Energy dispersive X-ray spectroscopy (EDS) is a surface chemical characterization technique which is used in conjunction with a scanning electron microscope (SEM). This spectroscopic technique bombards a sample with mono-energetic electron beam; these electrons then can eject secondary electrons from the core atomic orbitals [23]. Vacancies are created and filled electron from a higher orbital thus giving off characteristic X-rays from the energy gap, shown in Figure 14. The spectrum of X-ray intensity versus incident electron beam energy is then gathered.

The films were measured with a JEOL JSM-6500F SEM equipped with an EDS. An ultra-high vacuum is also required for these measurements.

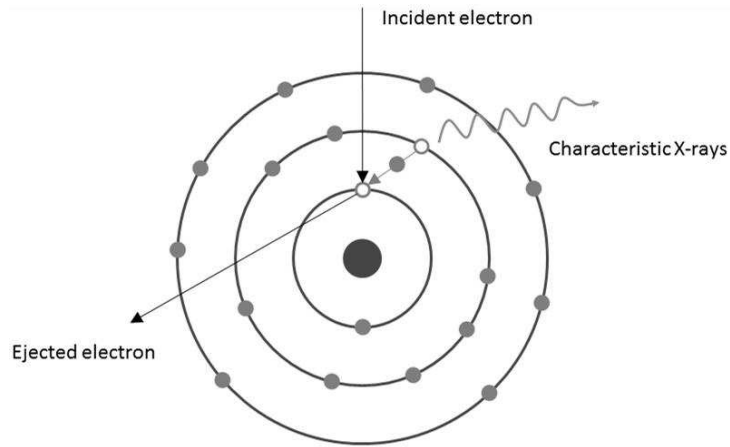


Figure 14: The working principle of EDS is shown for an arbitrary atom [23]. Incident electron beam knocks out inner core electrons, thus emitting x-ray which is characteristic of the energy gap.

#### 2.4.3 THIN-FILM STRESS FROM CARRIER FREQUENCY INTERFEROMETRY (CIF)

Thin-film coatings can have intrinsic or extrinsic stress due to deposition conditions or differences in thermal expansion with the substrate. Often, IBS films have high intrinsic compressive stress due to the high energy nature of the deposition process [3,4]. A carrier frequency interferometry system, developed at CSU, was used to characterize the thin-film stress [24]. This technique is capable of measuring a wave-front radius-of-curvature ( $R$ ) with an error of 0.2% for  $R < 500\text{m}$  [24]. The basic interferometer setup is displayed in Figure 15.

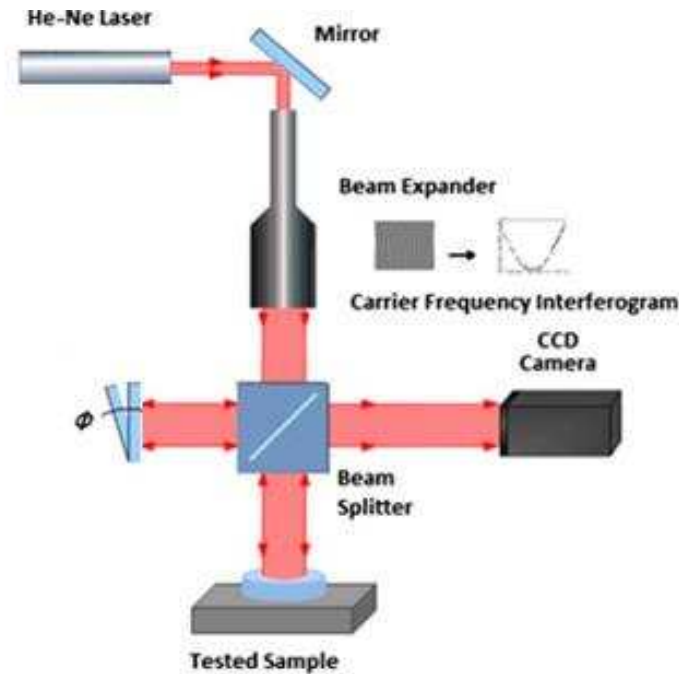


Figure 15: Diagram of the carrier frequency interferometer (CFI) optical system [24].

A frequency stabilized HeNe laser beam is telescoped to ~2inch diameter. This beam is split with a 50% beam splitter; one beam is directed toward a reference plate while the other is directed toward the sample. These two beams are reflected and again combine within the beam splitter creating an interferogram which is recorded on a CCD camera. A tilt about one axis of the sample or reference optic induces a linear carrier upon the orthogonal axis. If the sample and reference have equal surface curvature, then straight fringes will be produced. However, if the sample is not flat (which is often the case) the fringes produced will have a phase modulation due to the wave-front deformation. The wave-front is recovered through an inverse fast Fourier transform (FFT) and subsequent unwrapping procedure. Finally, the test sample's radius of curvature can be extracted through fitting the wave-front to a sphere. To extract the thin-film stress ( $\sigma_f$ ), Stoney's formula (displayed below) is used [3].

$$\sigma_f = \frac{Y_s \cdot d_s^2}{6R(1 - \nu_s)d_f}$$

Where  $\sigma_f$  is thin-film stress,  $Y_s$  is Young's modulus of the substrate,  $d_s$  is the thickness of the substrate,  $d_f$  is the thickness of the thin-film,  $R$  is the radius of curvature of the sample, and  $\nu_s$  Poisson's ratio of the substrate. It is important to note that this equation only holds valid for:  $R/d_s > 5$ .

For these measurements, each coating set was also deposited upon a 0.508mm thick fused silica stress witness samples purchased from Blue Ridge. The substrates were also tested for radius of curvature and were found to be  $>280\text{m}$ ; this is  $>5\text{x}$  the typical radius after thin-film deposition. This substrate was used to stay within the validity region of Stoney's equation. In order to mitigate back reflection of the transparent thin-films, a thin diffusion tape was placed on the back of the sample. This tape has been shown not to adversely affect the radius of curvature measurement. Several interferogram pictures were taken per sample and the results were averaged. For annealing, the same procedure was followed as described above, however extra care was taken to place the stress witness samples, thin-film side up, on a flat plate during annealing.

#### 2.4.4 LASER INDUCED DAMAGE THRESHOLD (LIDT)

As described in the previous chapters, the laser induced damage threshold (LIDT) of thin-film coatings for high-energy laser applications is of considerable importance. Understanding this laser damage process and threshold values for coatings help plan and scale the laser system. Further, correlating the LIDT and damage morphology with deposition conditions and coating designs helps scientist and engineers understand the basic physics of light-material interaction and advance coating technology.

The LIDT system, shown schematically in Figure 16, has six main sections.

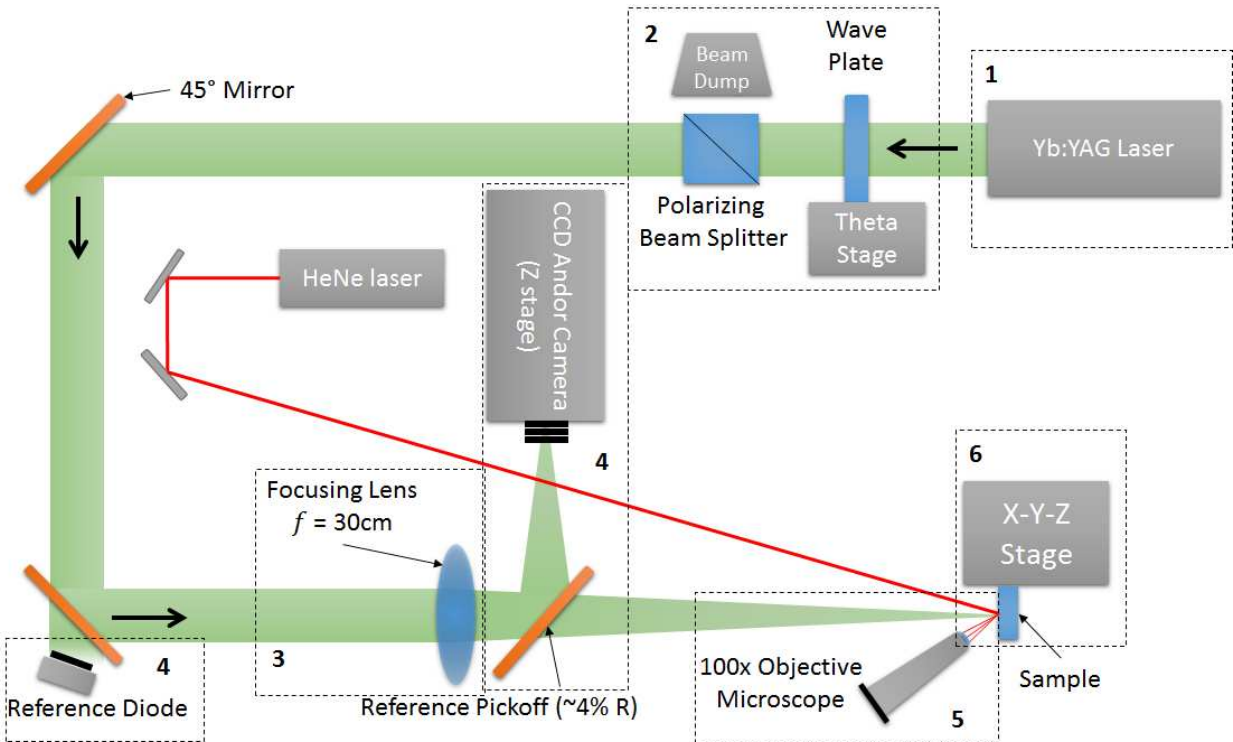


Figure 16: Diagram of the LIDT optical system (not to scale). The 5 main sections of the setup are described within the text.

1. The first section is the Yb:YAG laser system and is described in more detail in the following paragraphs. This laser has a center wavelength  $\lambda = 1030\text{nm}$  and produces trains of pulses (at 40Hz) of 220ps and 9ps. A Stanford DG645 delay generator and Newport electronic shutter, which were controlled with Matlab, were used to select 1 or 500 pulses from the laser.
2. The second section is comprised of a  $\frac{1}{2}$  wave plate and polarizing beam splitter. This set of optics act as a variable attenuator and give precise control over the energy or fluence of each laser pulse. Changing the wave-plate angle ( $\theta$ ) alters the linear polarization of the laser beam and the intensity transmitted through the polarizing beam splitter. The transmission of the beam splitter is set to be “P” polarization; this polarization was delivered to the samples during the LIDT test.

3. The third section is the focusing system. A single, 2inch diameter, plano-convex, AR coated lens with focal length  $f = 30\text{cm}$  was used. An f-number ( $f/\#$ ) = 60 was used. The  $f/\#$  or input diameter is chosen such that a  $100\mu\text{m}$  focal spot is created.
4. The fourth section of the LIDT system is the beam diagnostic unit. This unit consists of the Andor iKon CCD camera (cooled to  $-20^\circ\text{C}$ ) and Newport InGaAs photodiode (with 175ps rise time). A photodiode is positioned behind one mirror to observe the pulse width on an oscilloscope during the experiment. Part of the laser (<5%) is picked off after the focusing lens and directed toward the Andor camera. This is used for capturing the focal spot image for each shot and calibrating the energy (further discussed below).
5. The fifth unit in the LIDT system is damage detection. A 100x long working distance (WD = 13mm) microscope objective is focused at the sample under test. Due to practical issues, the objective is positioned out of the working distance and the image is relayed with additional lenses to achieve a focused image. A HeNe probe laser is used to produce scatter and illuminate the damage spot.
6. Finally, the sixth unit is the sample stage. The sample is held on a motorized X-Y stage and non-motorized Z stage. These motors are capable of a resolution of 0.01mm and have little jitter. Most of the laser spot lateral movement is due to laser jitter and air currents. These experiments were done in air at atmospheric conditions. Special care was taken to insure dust and contaminants did not alter the measurements.

A picture of the laser damage setup in the laboratory is displayed in Figure 17.

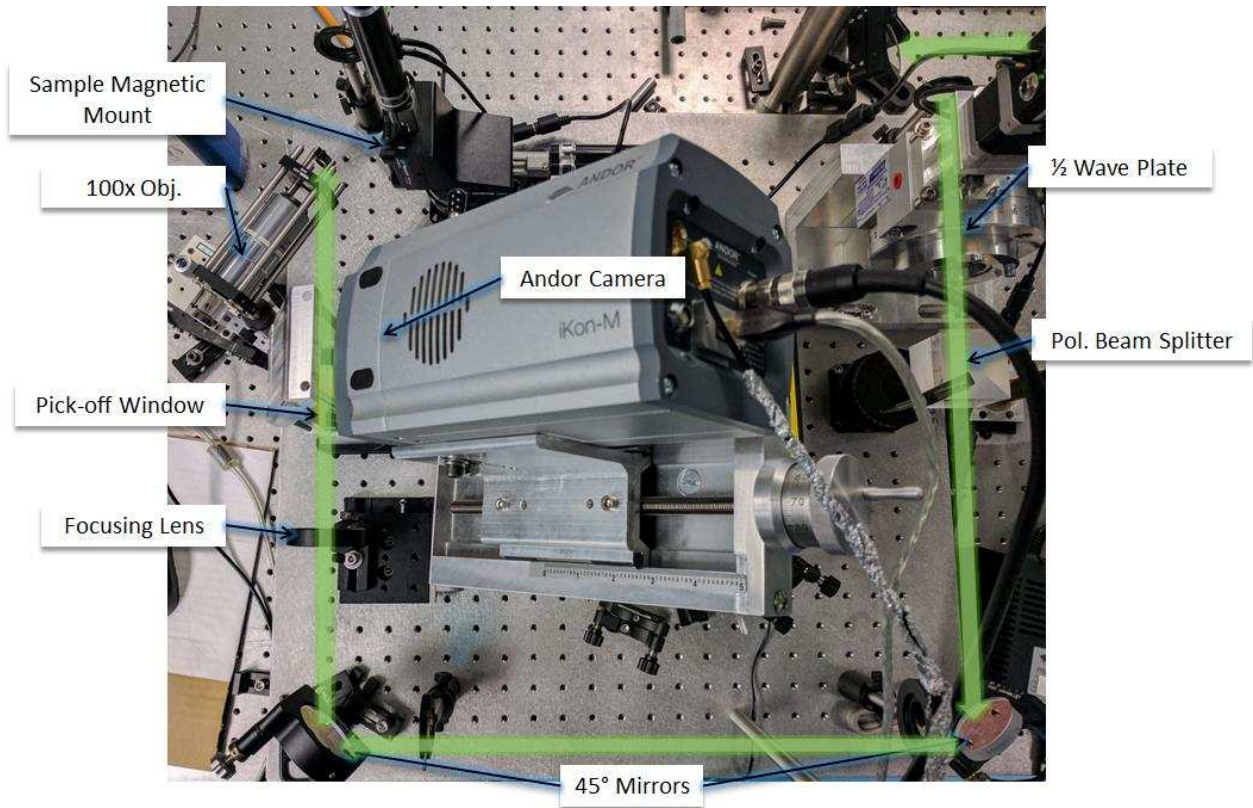


Figure 17: “Bird’s eye” picture of the laser damage system in the laboratory. The green line shows the laser path.

Before testing any samples, an energy calibration is performed. The consisted of measuring the pulse energy with a Newport 2936-R power meter while several focal spot images, at various pulse energies, were taken with the Andor camera. The images were cropped around the focal spot, background subtracted, Gaussian fit, and the counts are integrated. This is then plotted and fit, as shown in Figure 18.

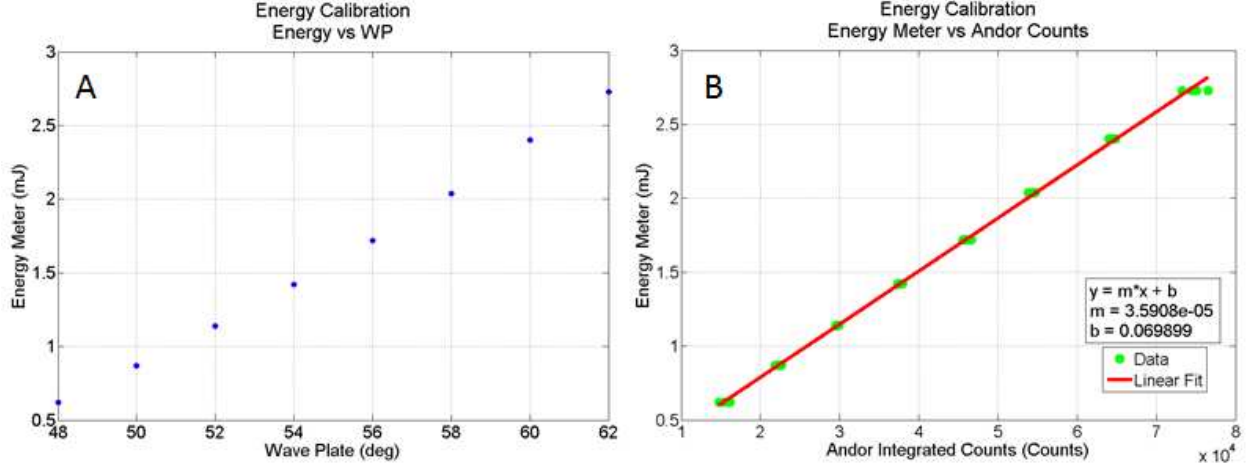


Figure 18: Example of results from an energy calibration. (A) shows the pulse energy versus wave plate angle. (B) shows the pulse energy versus Andor CCD Gaussian fit counts. The linear fit is used within the LIDT test to calculate energy from each laser shot.

The linear fit is used within the following LIDT tests to calculate energy from each laser shot. The spot diameter is measured at  $e^{-2}$  with a Gaussian fit. These values are then used to calculate individual shot fluence according to the equations:

$$A_{T,eff} = 2\pi \int_0^{\infty} e^{\frac{-8r^2}{d_{86.5}^2}} \cdot r \, dr = \frac{\pi d_{86.5}^2}{8}$$

$$F = \frac{E}{A_{T,eff}}$$

Where  $A_{T,eff}$  is the effective laser spot area,  $d_{86.5}$  is the laser spot diameter calculated with Gaussian at  $e^{-2}$  diameter,  $F$  is the fluence ( $\text{J}/\text{cm}^2$ ), and  $E$  is the pulse energy (mJ).

A graphical user interface (GUI) was developed in Matlab and was used for data acquisition, timing, moto movements, and calculations. Using computer control helps reduce human caused errors and increase sensitivity and repeatability. The LIDT method for this thesis follows the ISO 21254 standard, with the exception of the spot size and f-number requirements; which are:  $f/\# > 50$  and focal spot diameter  $> 0.8\text{mm}$  [25]. Due to the probabilistic nature of laser damage of defect within the coating, the damage versus fluence plot is rarely deterministic. Thus, it is necessary to test a large number of locations, at varying fluence, on the sample surface. For each fluence level, 20 single (1-on-1)

shots were delivered to the sample with a spacing of 0.75mm, as shown in Figure 19. In best practice, >2 fluences at which the damage statistic (number of damage sites/number of sites tested) is each 0% and 100%. Additionally, adequate number and resolution of fluences between these two 0% and 100% is also tested. In total >200 total spots will be tested on a given sample. The LIDT is calculated as the highest fluence for which the damage statistic is 0%. In other words, this is the highest fluence the optic can withstand without damaging (for the sites and total area tested). It is important to note that this method of LIDT testing has a reasonably high error solely due to the probabilistic nature of defect initiated laser damage and the relative low area tested. This has motivated many researchers within the community to develop new methods of LIDT testing [26-31]. An example of a laser damage probability plot is shown in Figure 19B below.

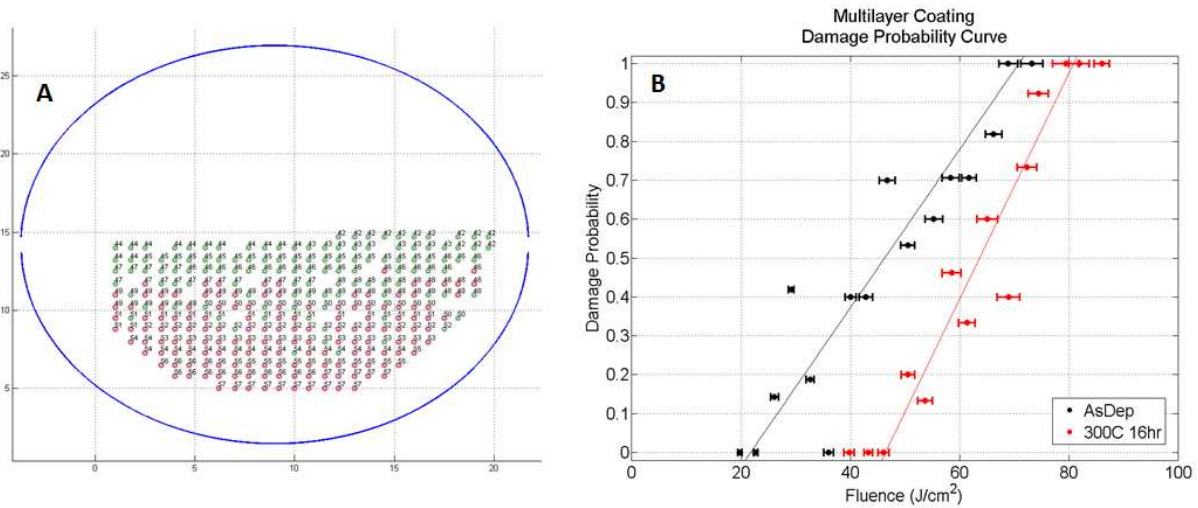


Figure 19: Part (A) shows a damage map on an arbitrary sample. Part (B) shows an example of a damage probability curve for a multilayer HR coating.

The stability, laser wavelength, pulse duration, and temporal and spatial profile are important parameters in LIDT experiments. For these experiments, a CSU built Yb:YAG cryo-cooled, diode pumped, solid state laser (lasing at 1030nm) was used [32]. The upstream end of the laser is a diode pumped, mode locked Yb:KYW oscillator emitting ~200fs pulses at 1030nm. These pulses are stretched to ~200ps

with a grating pulse stretcher. The stretched pulses are then seeded into an Yb:YAG diode pumped regenerative amplifier operating at room temperature. Once gain saturation is reached, the pulse is kicked out of the cavity with a Pockels cell and is subsequently “cleaned-up” (where any pre or post-pulses are clipped out) with a second Pockels cell. The laser beam is then routed through a diode pumped and cryo-cooled 2<sup>nd</sup> amplifying stage. This Yb:YAG amplifying stage is an active mirror design with 4 total passes (8 total amplifications). At optimum conditions the 2<sup>nd</sup> stage is capable of outputting >70mJ at 1Hz or ~40mJ at 100Hz. For laser damage uses, the laser is set to ~10mJ at 40Hz. Under optimum conditions, the typical pulse to pulse deviation is < 3%. For LIDT tests, the typical shot to shot sample standard deviation (STD) is  $\leq 0.5 \text{ J/cm}^2$ .

For short pulse LIDT testing, a laser compressor was built. The laser compressor is folded within a ~3.5 x ~4.5 foot vacuum chamber where two 20cm x 15cm gratings are housed. Out of the 2<sup>nd</sup> stage the laser is telescoped to ~50mm diameter and aligned through the compressor. Slight adjustments to the laser stretcher are made to reach a minimum of ~5ps pulse duration. For these experiments, achieving <10ps is sufficient.

The general laser and LIDT conditions are reviewed within Table 2a and 2b, below.

Table 2: Table 2a and 2b show the laser operation conditions and LIDT test methods conditions, respectively.

<b>(A) Laser Conditions</b>				
<b>Wavelength (nm)</b>	<b>Pulse Width (ps)</b>	<b>Rep Rate (Hz)</b>	<b>2<sup>nd</sup> Stage Pump Current (A)</b>	<b>Laser Energy</b>
1030nm	220ps & 9ps	40Hz	60A – 100A	< 10mJ

<b>(B) LIDT Conditions</b>						
<b>Spot Size (e<sup>-2</sup>)</b>	<b>Damage Standard</b>	<b>Damage Sites/Fluence</b>	<b>Spacing Between Sites</b>	<b>Damage Detection</b>	<b>Lens Focal Length (cm)</b>	<b>Testing Angle</b>
100 $\mu\text{m} \pm 5\mu\text{m}$	1-on-1 500-on-1	20	0.75mm	100x Microscope	30cm	Normal (<1°)

## REFERENCES

1. Macleod, H. Angus. *Thin-film optical filters*. CRC press, 2001.
2. Macleod, Angus, and Christopher Clark. "Optical coating design with the essential macleod." (2012).
3. Ohring, Milton. *Materials science of thin films*. Academic press, 2001.
4. Cuomo, Jerome J., Stephen M. Rossnagel, and Harold R. Kaufman. "Handbook of ion beam processing technology." (1989).
5. Krous, Erik M. *Characterization of Scandium Oxide thin films for use in interference coatings for high-power lasers operating in the near-infrared*. Diss. Colorado State University. Libraries, 2010
6. Emmert, Luke A., Mark Mero, and Wolfgang Rudolph. "Modeling the effect of native and laser-induced states on the dielectric breakdown of wide band gap optical materials by multiple subpicosecond laser pulses." *Journal of Applied Physics* 108.4 (2010): 043523.
7. Markosyan, A. S., et al. "Study of spontaneous and induced absorption in amorphous Ta<sub>2</sub>O<sub>5</sub> and SiO<sub>2</sub> dielectric thin films." *Journal of Applied Physics* 113.13 (2013): 133104.
8. Menoni, Carmen S., et al. "Advances in ion beam sputtered Sc<sub>2</sub>O<sub>3</sub> for optical interference coatings." *Proc. SPIE*. Vol. 7842. 2010.
9. Langston, P. F., et al. "Point defects in Sc<sub>2</sub>O<sub>3</sub> thin films by ion beam sputtering." *Applied optics* 53.4 (2014): A276-A280.
10. Langston, Peter F. *A study of the influence of process parameter variations on the material properties and laser damage performance of ion beam sputtered Sc<sub>2</sub>O<sub>3</sub> and HfO<sub>2</sub> thin films*. Diss. Colorado State University, 2016.
11. Langdon, B., et al. "Electron spin resonance spectroscopy investigation of ion beam sputtered HfO<sub>2</sub> and SiO<sub>2</sub> thin films." *Proc. SPIE*. Vol. 7132. 2008.
12. Langston, Peter, et al. "SiO<sub>2</sub>/HfO<sub>2</sub> Multilayers: Impact of Process Parameters and Stack Geometry on the Optical and Structural Properties." *Frontiers in Optics*. Optical Society of America, 2008.
13. Langdon, B., et al. "Influence of process conditions on the optical properties HfO<sub>2</sub>/SiO<sub>2</sub> thin films for high power laser coatings." *Proc. SPIE*. Vol. 6720. 2007.
14. Stolz, Christopher J., et al. "High laser-resistant multilayer mirrors by nodular defect planarization [Invited]." *Applied optics* 53.4 (2014): A291-A296.
15. Stolz, Christopher J., et al. "Defect insensitive 100 J/cm<sup>2</sup> multilayer mirror coating process." *SPIE Laser Damage*. International Society for Optics and Photonics, 2013.
16. Stolz, Christopher J., et al. "Substrate and coating defect planarization strategies for high-laser-fluence multilayer mirrors." *Thin Solid Films* 592 (2015): 216-220.
17. Griscom, David L. "Optical properties and structure of defects in silica glass." *Journal of the Ceramic Society of Japan* 99.1154 (1991): 923-942.
18. Devine, R. A. B., and A. Golanski. "Creation and annealing kinetics of magnetic oxygen vacancy centers in SiO<sub>2</sub>." *Journal of Applied Physics* 54.7 (1983): 3833-3838.
19. Devine, R. A. B. "Oxygen vacancy creation in SiO<sub>2</sub> through ionization energy deposition." *Applied physics letters* 43.11 (1983): 1056-1058.

20. Arnold, G. W. "Ion-implantation effects in noncrystalline SiO<sub>2</sub>." *IEEE Transactions on Nuclear Science* 20.6 (1973): 220-223.
21. Alexandrovskika, Alexei, et al. "Photothermal common path interferometry (PCI): new developments." *Proc. of SPIE Vol. Vol. 7193*. 2009.
22. Watts, John F., and John Wolstenholme. "An introduction to surface analysis by XPS and AES." (2003).
23. Zhou, Weilie, and Zhong Lin Wang, eds. *Scanning microscopy for nanotechnology: techniques and applications*. Springer science & business media, 2007.
24. Jankowska, E., S. Drobczynski, and C. S. Menoni. "Analysis of surface deformation in thin-film coatings by carrier frequency interferometry." *Applied Optics* 56.4 (2017): C60-C64.
25. International Organization for Standardization, ISO-21254: Lasers and laser-related equipment- Test methods for laser-induced damage threshold (2011).
26. Bercegol, Herve. "Statistical distribution of laser damage and spatial scaling law for a model with multiple defects cooperation in damage." *Laser-Induced damage in Optical Materials: 1999 3902* (2000): 339-346.
27. Volto, Patricia, et al. "Refined statistical measurements of laser damage." *Laser-Induced Damage in Optical Materials: 1999*. International Society for Optics and Photonics, 2000.
28. Porteus, J. O., and Steven C. Seitel. "Absolute onset of optical surface damage using distributed defect ensembles." *Applied optics* 23.21 (1984): 3796-3805.
29. Xu, Yeji, Luke A. Emmert, and Wolfgang Rudolph. "Spatio-temporally resolved optical laser induced damage (STEREO LID) technique for material characterization." *Optics express* 23.17 (2015): 21607-21614.
30. Bercegol, Hervé, et al. "The impact of laser damage on the lifetime of optical components in fusion lasers." *XXXV Annual Symposium on Optical Materials for High Power Lasers: Boulder Damage Symposium*. International Society for Optics and Photonics, 2004.
31. Negres, Raluca A., et al. "Apparatus and techniques for measuring laser damage resistance of large-area, multilayer dielectric mirrors for use with high energy, picosecond lasers." *Lasers and Electro-Optics (CLEO), 2015 Conference on*. IEEE, 2015.
32. Baumgarten, Cory, et al. "1 J, 0.5 kHz repetition rate picosecond laser." *Optics letters* 41.14 (2016): 3339-3342.

## CHAPTER 3

### IMPACTS OF SiO<sub>2</sub> PLANARIZATION ON OPTICAL THIN-FILM PROPERTIES AND LASER DAMAGE

#### RESISTANCE

#### 3.1 INTRODUCTION

From the advent of the laser, laser-induced damage (LID) of various optical components has been a limiting issue for the development of modern higher power laser systems. Often nodules are the lowest fluence limiting defects of multilayer interference coatings [1-4]. These defects, created from surface deformations, scratches, dust, improper substrate cleaning, impurities, or coating flakes, cause large deformations in the coating surface which in turn induces light intensification leading to catastrophic coating damage and nodule ejection [1-8]. To address this common issue, particularly with large aperture optics, LLNL and CSU have co-developed a planarization surface smoothing process [9-12]. Planarization processing through ion bombardment and etching was originally developed to smooth substrate particles for extreme ultraviolet (EUV) multilayer mirrors and lithography [13,14]. This deposition process has the capability to smooth over micron-size nodules at the substrate surface or within the multilayer coatings. When applied to engineered nodular defects, a 20x improvement in the single-shot LIDT and 3x improvement in the multi-shot LIDT has been observed with control engineered coatings [9] Yet, when applied to real (non-engineered) coatings, the planarized mirrors have increased damage density per square centimeter raster scanned areas and damages with flat-bottomed interfacial damage craters with depths correlating to the top planarized SiO<sub>2</sub> layers [15]. The concept of planarization through ion bombardment and etching to smooth substrate particles was originally demonstrated in Si layers that compose extreme ultraviolet (EUV) multilayer mirrors for lithography [13,14]

This work describes results of the characterization of planarized SiO<sub>2</sub> samples aimed at identifying if the planarization process affects absorption loss, stress, and surface roughness compared to as deposited SiO<sub>2</sub>. The investigations also include an analysis of impurity content, specifically Ar and Mo, which could be likely embedded in the films due to the sputtering of the SiO<sub>2</sub> with the assist source. LIDT tests using 1-on-1 and 500-on-1 protocols were carried out to identify the effect of planarization. A second set of samples containing an additional layer of HfO<sub>2</sub> was grown and analyzed to identify whether the planarization process changed the optical and LIDT behaviors of a layer of HfO<sub>2</sub> that emulates the sequence of deposition in a multilayer structure.

### 3.2 EXPERIMENT

Planarization processing, discussed in depth elsewhere [11,12], involves multiple discrete grow and etch cycles, in a 2:1 ratio, to smooth nodular defects in SiO<sub>2</sub>. Within multilayer interference coatings, 8 planarization cycles are repeated (deposition then etch) per  $\lambda/4$  SiO<sub>2</sub> layer or until the desired thickness is reached.

The coatings were fabricated by dual ion beam sputtering (IBS) using a Veeco Spector<sup>®</sup> system and deposited upon super polished UV-grade fused silica substrates (0.5-mm-thick substrates were used in measuring the stress, otherwise 6.35-mm-thick laser damage substrates were used). A set of 350 nm ( $\lambda/2$  at 1030 nm) as deposited and planarized SiO<sub>2</sub> films were fabricated and 125 nm ( $\lambda/4$  at 1030 nm) HfO<sub>2</sub> films were then deposited upon a second set of these SiO<sub>2</sub> coatings. The SiO<sub>2</sub> films were sputtered from an oxide target and HfO<sub>2</sub> films from a metallic target using deposition and etching conditions of 1.25 keV ion energy and 600 mA current and, 1 keV ion energy and 150 mA current, respectively [8]. The SiO<sub>2</sub> is etched with 1 keV argon (Ar) ions accelerated through molybdenum (Mo) grids. These ions or grid material have the potential to implant into the film and alter the optical, micro-structural properties, or laser damage morphology. A diagram of the planarization process with discrete deposit and etch cycles is shown in Figure 20. Thin red bands represent the approximately 3 nm penetration

depth of 1 keV Ar ions into SiO<sub>2</sub> calculated from SRIM Monte Carlo modeling. The short penetration depth leads to small bands throughout the thickness of the coating where Ar implantation, Mo contamination, or other defects may lie.

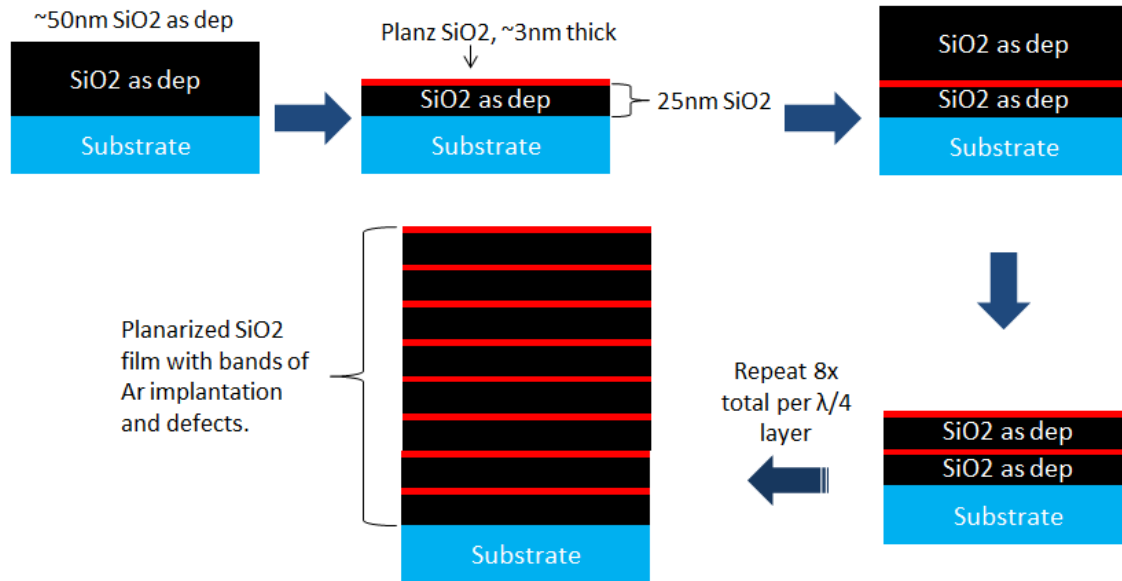


Figure 20: This diagram shows the steps involved in the planarization (planz) process. The red thin bands represent approximately 3 nm penetration depth of Ar ions.

The samples were characterized for their surface roughness using a Zygo Scanning White Light Interferometer (SWLI). The surface RMS roughness was measured at 5 unique and random locations throughout the film surface with 100x microscope objective. The axial resolution of the instrument is 0.11nm.

Stress in the thin films was determined from measurements of the radius of curvature of a 0.5 mm thick substrate onto which the amorphous thin films were deposited. The radius of curvature was measured using carrier frequency interferometry, a method recently demonstrated by our group [15]. Radius of curvature was related to stress via the Stoney's formula.

Photothermal common-path interferometry (PCI) [17] employing a 1064 nm Nd:YAG fiber amplified pump and 632.8 nm HeNe probe laser was used to measure absorption loss. Each sample was measured at 5 unique locations and the values averaged.

As pointed out above, the sequential deposition and etching of the planarization process leaves regions in the SiO<sub>2</sub> where an excess of Ar implantation or Mo contamination coming from the grids could be found. To analyze Mo and Ar content in the samples X-ray photoelectron spectroscopy (XPS) and energy-dispersive X-ray spectroscopy (SEM-EDS) implemented with a high-resolution PE-5800 XPS instrument with Cu K<sub>α</sub> radiation and a JEOL JSM-6500F SEM equipped with an electron energy dispersive X-ray spectrometer (EDS) respectively were used.

The LIDT characteristics are a critical feature in many optical components for high fluence applications. For the scope of this work, 1-on-1 and 500-on-1 LIDT measurements were carried out with a 100 μm (e<sup>-2</sup>) spot size and corresponding to ISO: 21254. The damaging laser was a 1030nm Yb:YAG mode-locked oscillator with a regenerative amplifier operating at 220ps and a fiber diode pumped, cryogenically cooled 2nd amplifying stage with 70 mJ output at 20 Hz [18]. Coating damage was detected with an *in situ* scatter microscope and *ex situ* Nomarski microscope at 40x and 100x. Figure 21 displays the optical setup for LIDT testing.

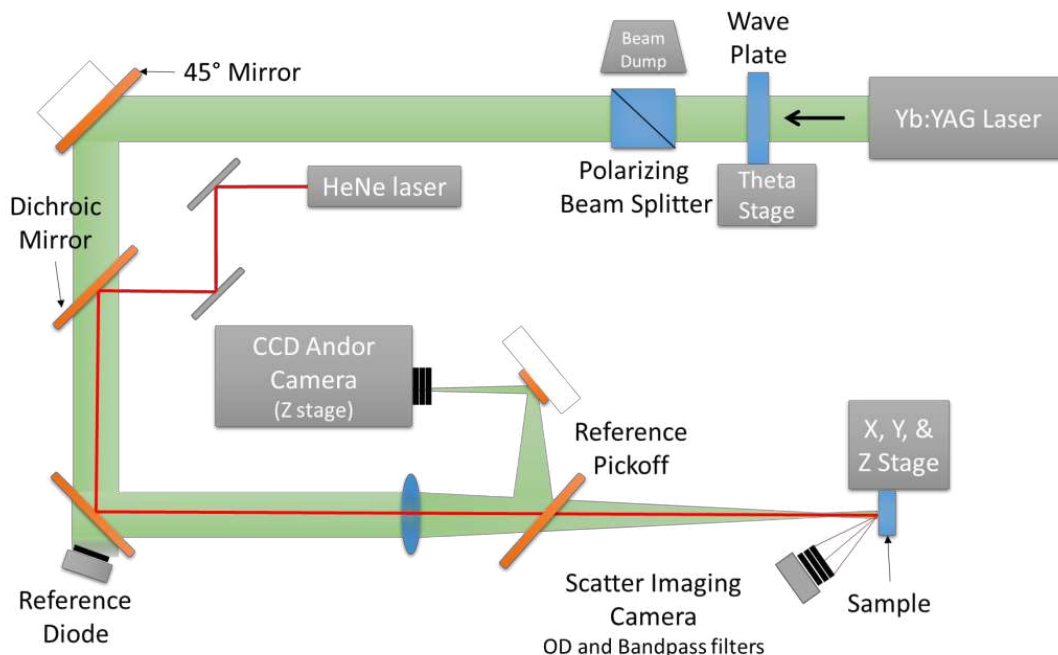


Figure 21: Schematic diagram of laser damage setup.

### 3.3 RESULTS

Table 3: A summary of the coating samples tested, thickness, surface roughness, thin film stress, and absorption loss. The uncertainties reported are calculated using corrected sample standard deviation.

Sample	Thickness (nm)	RMS Surface Roughness (Å)	Film Stress (MPa)	PCI Absorption Loss (ppm)
UV grade Fused Silica	N/A	$2.8 \pm 0.5 \text{ \AA}$	N/A	28.1 ppm/cm
SiO <sub>2</sub> as dep	350 nm	$2.9 \pm 0.6 \text{ \AA}$	$\delta = 275 \text{ MPa}$	$5.70 \pm 0.08 \text{ ppm}$
SiO <sub>2</sub> planarized	350 nm	$3.3 \pm 0.1 \text{ \AA}$	$\delta = 231 \text{ MPa}$	$17.2 \pm 0.2 \text{ ppm}$
HfO <sub>2</sub> / SiO <sub>2</sub> as dep	125 nm / 350 nm	N/A	$\delta = 225 \text{ MPa}$	$8.0 \pm 0.2 \text{ ppm}$
HfO <sub>2</sub> / SiO <sub>2</sub> planarized	125 nm / 350 nm	N/A	$\delta = 212 \text{ MPa}$	$18.5 \pm 0.3 \text{ ppm}$
HfO <sub>2</sub> single	125 nm	N/A	N/A	$5.1 \pm 0.1 \text{ ppm}$

Table 3 summarizes the thin film samples tested and their respective thickness, surface roughness, thin film stress, and absorption loss. It was found the RMS surface roughness is slightly increased by ~13% from as deposited SiO<sub>2</sub> and ~16% from the polished substrate. Yet, the roughness is still well within acceptable parameters for optical performance. Incidentally, planarization is optimized to smooth large, micron-sized contaminates and nodules yet, has little to no effect on RMS roughness

when utilized without these defects present. The SiO<sub>2</sub> planarized has approximately -18% change in the thin film stress as compared with the SiO<sub>2</sub> as deposited. While the HfO<sub>2</sub> capped SiO<sub>2</sub> films slightly less stress than the single SiO<sub>2</sub>.

The SiO<sub>2</sub> planarized and HfO<sub>2</sub> capped SiO<sub>2</sub> planarized coatings have a 3x and 2.3x increase in absorption loss compared to as deposited SiO<sub>2</sub>, respectively. This observation prompted further characterization techniques to uncover the cause of this absorption increase. These films were also annealed at 300°C for 8 hours in air at atmospheric pressure. An improvement in the absorption loss of the coatings is shown in Figure 22.

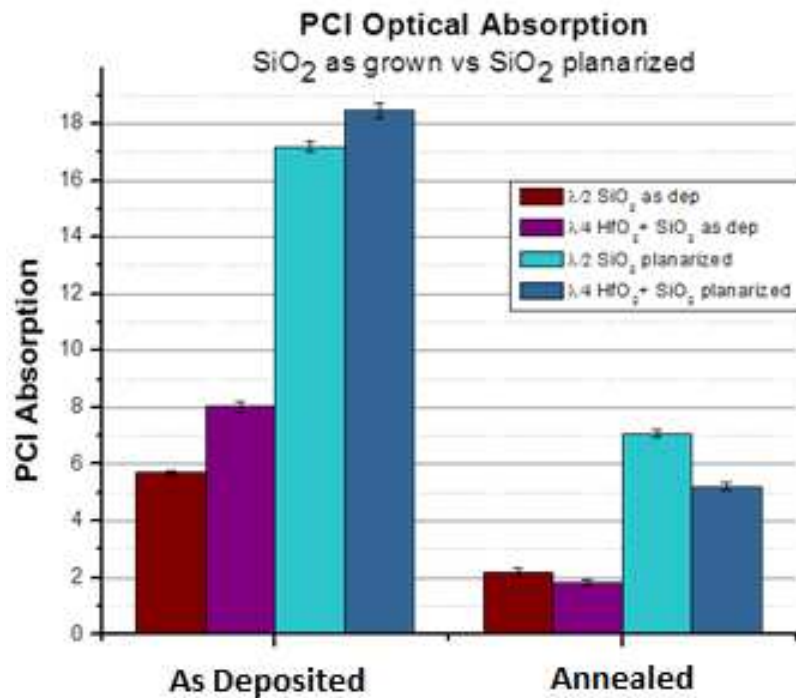


Figure 22: Bar graph comparing PCI absorption (ppm) of SiO<sub>2</sub> as deposited, SiO<sub>2</sub> planarized and HfO<sub>2</sub> capped SiO<sub>2</sub> films. Right shows the absorption loss decreases after annealing at 300°C for 8 hours.

With XPS there were no peaks found at the 3d5/2 photoelectron of metallic Mo in both SiO<sub>2</sub> films and a small amount of implanted Ar, at the 2p1/2 photoelectron line, was found within the planarized SiO<sub>2</sub> film only. As Figure 23 shows, there is less Mo than the minimum detectable limit of XPS,

of about part per thousand. Complimentary full elemental EDS scans and high-resolution scans around the known lines of Mo and Ar were carried out and are shown in Figure 24. Even with adequately long counting times the Mo  $L_{\alpha}$  and Ar  $k_{\alpha}$  lines at 2.293 keV and 2.957 keV, respectively, peaks have very little form and scarcely rise above the continuum background noise. It is believed that there are insignificant amounts of contamination detected to be a considerable factor in the increased absorption or laser damage morphology.

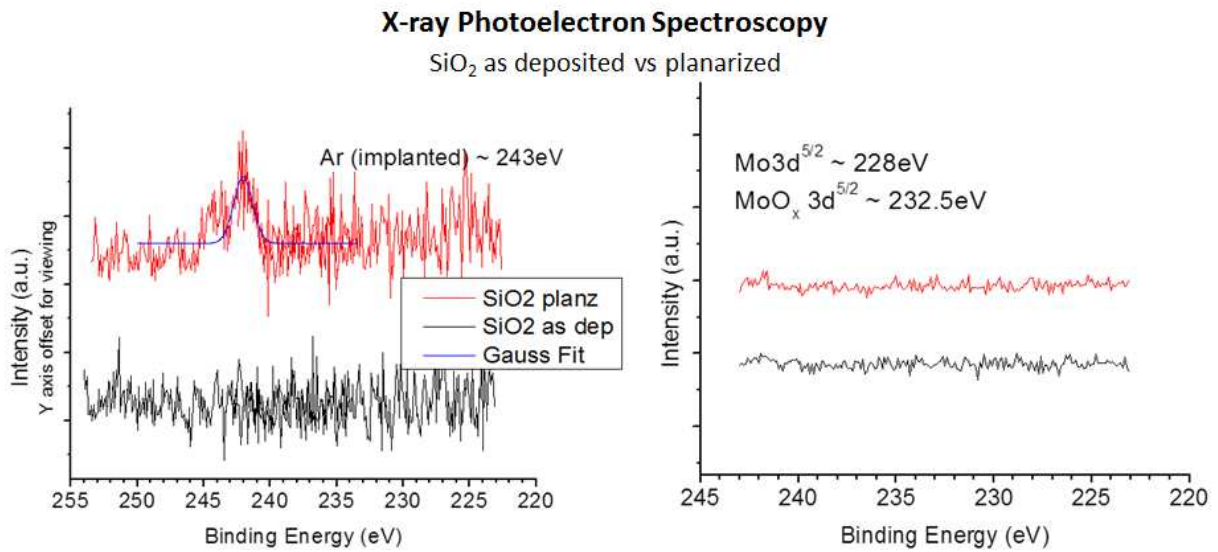


Figure 23: XPS data comparing SiO<sub>2</sub> as deposited vs planarized.

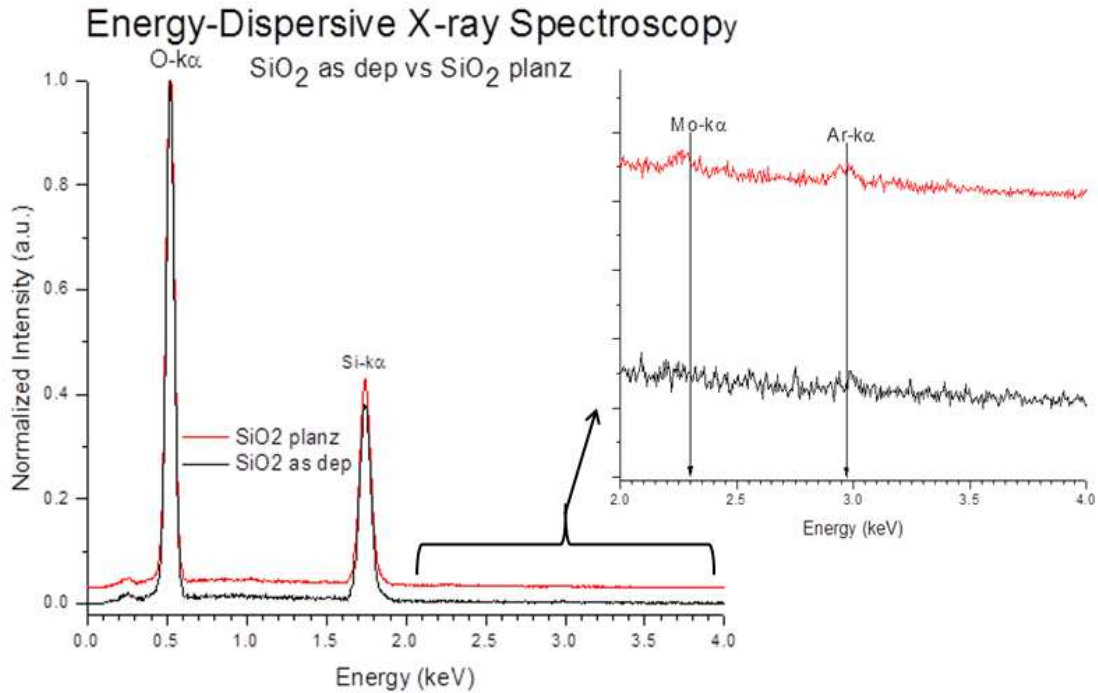


Figure 24: SEM-EDS comparing SiO<sub>2</sub> as deposited vs planarized.

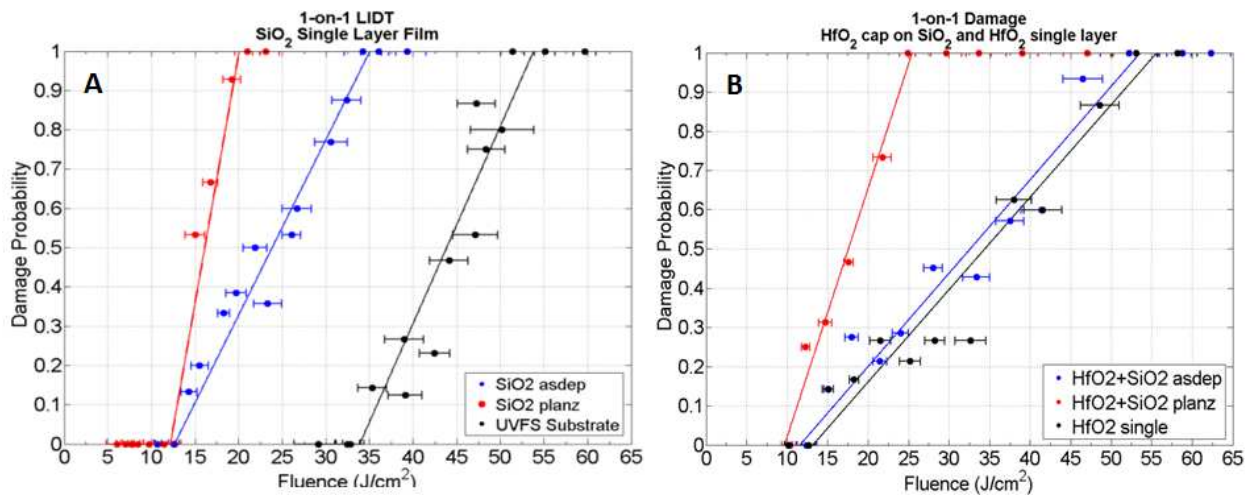


Figure 25: LIDT probability data showing 1-on-1 damage at 1030nm and 220ps of (A) SiO<sub>2</sub> single layers (as deposited and planarized) and UV grade fused silica substrate and (B) HfO<sub>2</sub> capped SiO<sub>2</sub> films and HfO<sub>2</sub> single layers. Error bars correspond to the standard deviation error calculated from variations in pulse energy and spot size.

The 1-on-1 LIDT results, Figure 25, showed similar onset fluences for all films of about 11-13 J/cm<sup>2</sup>, yet both SiO<sub>2</sub> planarized coatings have steeper sloped damage probability curves. For laser

damage resistance, HfO<sub>2</sub> is often claimed to be the limiting material in multilayer coatings, [22] however it is not the case here. A 20-40% decrease in the 50% and 100% damage probabilities of planarized SiO<sub>2</sub> and HfO<sub>2</sub> capped planarized SiO<sub>2</sub> was observed. For comparison, the UV grade fused silica substrate was also LIDT tested and has an onset fluence of about 33 J/cm<sup>2</sup>. The sharp LID probability curves signify a greater density of nano-absorber defects throughout the entire film.

The damage morphology, Figure 26, shows damage pitting as small as ~3 μm in diameter at damage onset fluences. These pits accumulate at higher fluences. In most cases, the planarized SiO<sub>2</sub> coatings have larger density of damage pits in the irradiated area, at the same damage probability fluence. HfO<sub>2</sub> capped SiO<sub>2</sub> exhibited in a similar damage morphology trend. This damage morphology has been previously linked to nano-absorption induced LID initiation [23-25]. Further, this damage morphology was seen by L. Gallais et al. in HfO<sub>2</sub> single layers and effectively modeled by metallic Hf and non-stoichiometric HfO<sub>2</sub> inclusions [23]

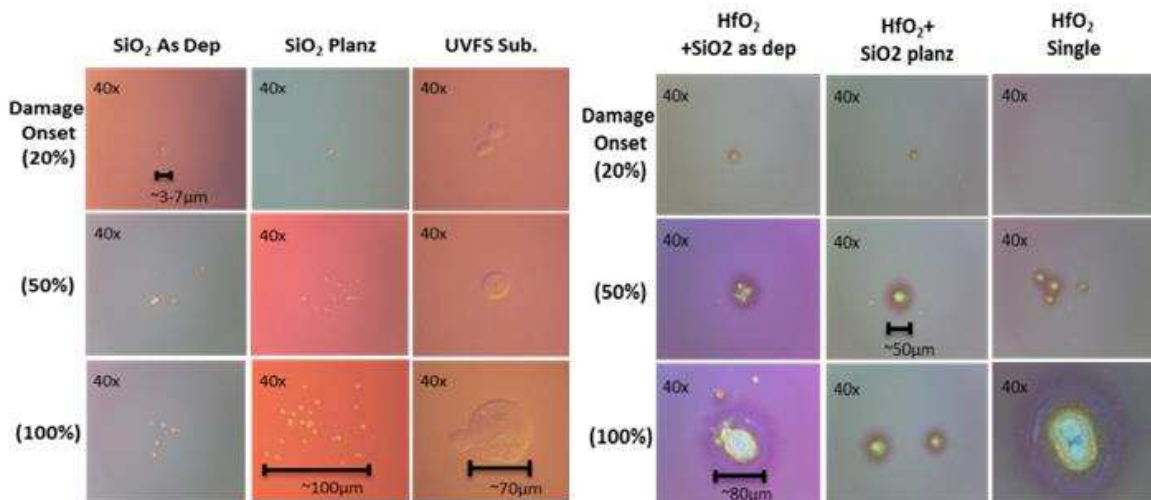


Figure 26: Nomarski images characteristic damage craters at damage onset, 50% damage, and 100% damage for SiO<sub>2</sub> films and HfO<sub>2</sub> capped SiO<sub>2</sub> films.

To investigate laser induced damage growth of these samples, 500-on-1 LIDT measurements were completed. Figure 27A displays the damage probability curve with and without growth and damage craters. It was observed, in Figure 27B, that low fluence damage does not grow with successive

pulses. The damage growth region begins around 30–35 J/cm<sup>2</sup> and produces approximately 400 μm damage craters which penetrate the substrate. Additionally, the diameter of these craters and density of pits within the irradiated area increase with higher fluences. Within the non-growth region, planarized SiO<sub>2</sub> again damaged with a higher density of damage pitting. As discussed above, this damage pitting is likely linked to nano-absorber initiation sites consisting of metallic bonds or oxygen deficiency defects.

### 3.4 CONCLUSION

In this work, the optical, micro-structural properties, and laser damage resistance of IBS SiO<sub>2</sub> as grown and planarized have been investigated. It was found the absorption loss of planarized SiO<sub>2</sub> films is about 3x that of the control samples and post-annealing decreases these losses. Insignificant amounts of Mo and Ar contamination was found and a ~18% reduction in the stress was observed. LIDT measurements show both SiO<sub>2</sub> and HfO<sub>2</sub> coatings damage at similar fluences, yet planarized SiO<sub>2</sub> coatings have steeper sloped damage probability curves. The steep LID probability curves, increased damage pitting morphology, and increased absorption which decreases after annealing indicate metallic bonds or oxygen deficiency nano-absorption sites as probable candidates for damage in planarized SiO<sub>2</sub> films. This could be the result of preferential oxygen etching during planarization. High energy (10's keV) ion implantation has been observed to create various oxygen deficiency point defects and annealing was shown to recover these defects [19,20] Additional photothermal microscopy has been used to observe nano-absorption laser damage precursors [21]. It is likely that these nano-absorber defects are playing a major role in the film absorption. This possible scenario is supported by PCI results on the annealed samples.

Overall, the results of this work show planarization processing, which is effective in mitigating low fluence nodular defects in optical interference coatings, does not significantly affect the microstructure, the optical properties, or the LIDT when tested at 1030 nm wavelength and 220ps pulse duration.

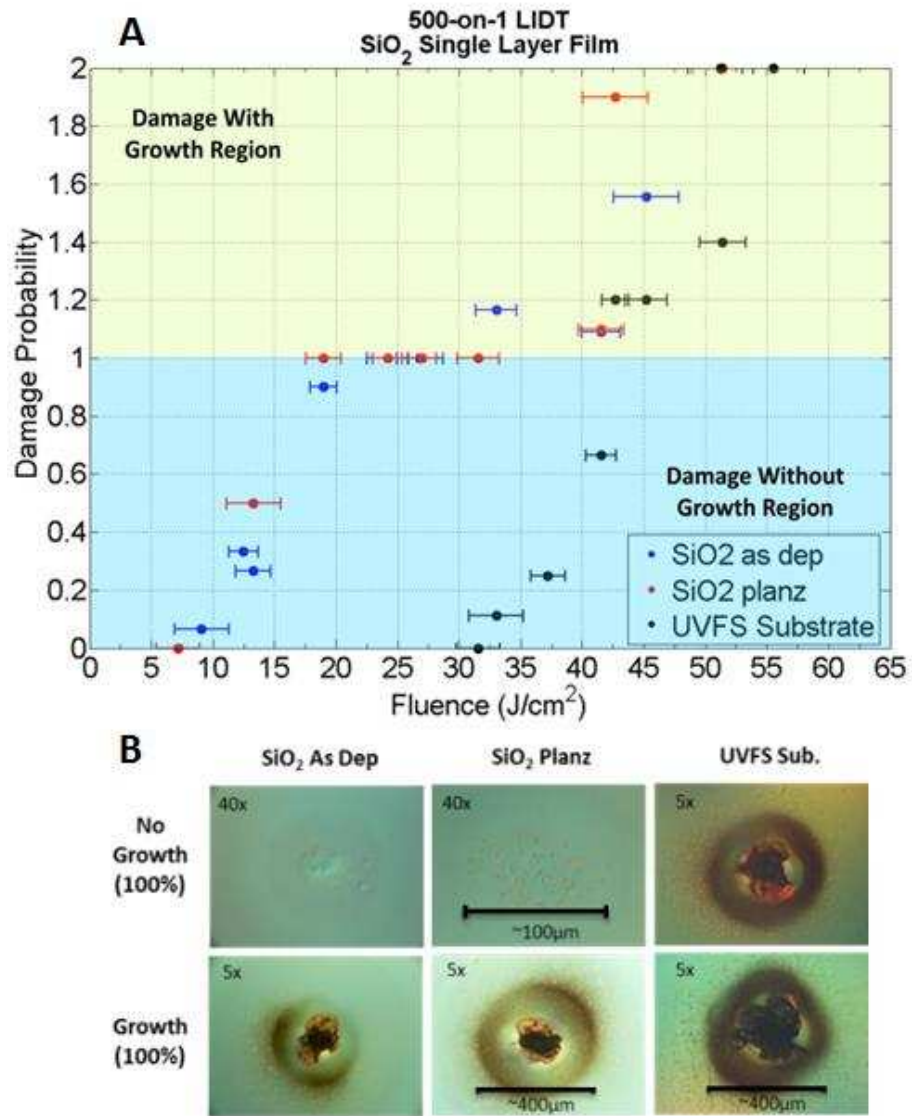


Figure 27: (A) LIDT probability data showing 500-on-1 damage of SiO<sub>2</sub> single layers (as deposition and planarized) and UV grade fused silica substrate. The region between 0 and 1 damage probability indicates damage which does not grow whereas the region between 1 and 2 damage probability indicates damage which grows with successive pulses. (B) Nomarski images characteristic damage craters at 100% damage without growth and 100% damage with growth for SiO<sub>2</sub> films.

## REFERENCES

1. Guenther, Karl H. "Nodular defects in dielectric multilayers and thick single layers." *Applied optics* 20.6 (1981): 1034-1038.
2. Stolz, Christopher J., et al. "Comparison of nodular defect seed geometries from different deposition techniques." *Laser-Induced Damage in Optical Materials: 1995*. International Society for Optics and Photonics, 1996.
3. Cheng, Xinbin, et al. "Laser damage study of nodules in electron-beam-evaporated HfO<sub>2</sub>/SiO<sub>2</sub> high reflectors." *Applied optics* 50.9 (2011): C357-C363.
4. Cheng, Xinbin, et al. "Nanosecond laser-induced damage of nodular defects in dielectric multilayer mirrors [Invited]." *Applied optics* 53.4 (2014): A62-A69.
5. DeFord, J. F., and Mark R. Kozlowski. "Modeling of electric-field enhancement at nodular defects in dielectric mirror coatings." *Optical Materials for High Power Lasers*. International Society for Optics and Photonics, 1993.
6. Cheng, Xinbin, et al. "The effect of an electric field on the thermomechanical damage of nodular defects in dielectric multilayer coatings irradiated by nanosecond laser pulses." *Light: Science & Applications* 2.6 (2013): e80.
7. Cheng, Xinbin, et al. "Physical insight toward electric field enhancement at nodular defects in optical coatings." *Optics express* 23.7 (2015): 8609-8619.
8. Qiu, S. Roger, et al. "Impact of substrate surface scratches on the laser damage resistance of multilayer coatings." *Laser Damage Symposium XLII: Annual Symposium on Optical Materials for High Power Lasers*. International Society for Optics and Photonics, 2010.
9. Stolz, Christopher J., et al. "Defect insensitive 100 J/cm<sup>2</sup> multilayer mirror coating process." *SPIE Laser Damage*. International Society for Optics and Photonics, 2013.
10. Stolz, Christopher J., et al. "High laser-resistant multilayer mirrors by nodular defect planarization [Invited]." *Applied optics* 53.4 (2014): A291-A296.
11. Stolz, Christopher J., et al. "Substrate and coating defect planarization strategies for high-laser-fluence multilayer mirrors." *Thin Solid Films* 592 (2015): 216-220.
12. C. J. Stolz, J. A. Folta, P. B. Mirkarimi, R. Soufli, C. C. Walton, J. E. Wolfe, C. S. Menoni, D. Patel, "Planarization of multilayer optical coating defects," Provisional Patent Attorney Docket Number IL-12580 (2012).
13. Mirkarimi, P. B., et al. "A silicon-based, sequential coat-and-etch process to fabricate nearly perfect substrate surfaces." *Journal of nanoscience and nanotechnology* 6.1 (2006): 28-35.
14. Mirkarimi, P. B., et al. "Advancing the ion beam thin film planarization process for the smoothing of substrate particles." *Microelectronic engineering* 77.3 (2005): 369-381.
15. Stolz, Christopher J., et al. "Depth determination of critical fluence-limiting defects within planarized and non-planarized mirror coatings." *SPIE Optical Systems Design*. International Society for Optics and Photonics, 2015.
16. Jankovska, Elzbieta, Slawomir Drobczynski, and Carmen S. Menoni. "Analysis of surface deformation by carrier frequency interferometry." *Optical Interference Coatings*. Optical Society of America, 2016.
17. Alexandrovski, Alexei, et al. "Photothermal common-path interferometry (PCI): new developments." *SPIE LASE: Lasers and Applications in Science and Engineering*. International Society for Optics and Photonics, 2009.
18. Baumgarten, Cory, et al. "1 J, 0.5 kHz repetition rate picosecond laser." *Optics Letters* 41.14 (2016): 3339-3342.

19. Devine, R. A. B., and A. Golanski. "Creation and annealing kinetics of magnetic oxygen vacancy centers in SiO<sub>2</sub>." *Journal of Applied Physics* 54.7 (1983): 3833-3838.
20. Devine, R. A. B. "Oxygen vacancy creation in SiO<sub>2</sub> through ionization energy deposition." *Applied physics letters* 43.11 (1983): 1056-1058.
21. Commandré, Mireille, J-Y. Natoli, and Laurent Gallais. "Photothermal microscopy for studying the role of nano-sized absorbing precursors in laser-induced damage of optical materials." *The European Physical Journal Special Topics* 153.1 (2008): 59-64.
22. Kaiser, Norbert, and Hans K. Pulker, eds. *Optical interference coatings*. Vol. 88. Springer, 2013.
23. Gallais, Laurent, et al. "Investigation of nanodefekt properties in optical coatings by coupling measured and simulated laser damage statistics." *Journal of Applied Physics* 104.5 (2008): 053120.
24. Papernov, S., and A. W. Schmid. "Correlations between embedded single gold nanoparticles in SiO<sub>2</sub> thin film and nanoscale crater formation induced by pulsed-laser radiation." *Journal of Applied Physics* 92.10 (2002): 5720-5728.
25. Batavičiutė, Gintarė, et al. "Revision of laser-induced damage threshold evaluation from damage probability data." *Review of Scientific Instruments* 84.4 (2013): 045108.

## CHAPTER 4

### THIN-FILM PLANARIZATION OF SINGLE AND MULTILAYERS AT PULSE DURATIONS OF 9PS AND 220PS

#### 4.1 INTRODUCTION

The laser damage resistance of multilayer laser mirrors, designed for use around  $\lambda = 1\mu\text{m}$  and long pulse durations (ns to >20ps) is often limited by nodular defects [1-4]. To mitigate this common issue, a surface planarization process was developed and originally used to smooth surfaces of Mo/Si multilayer coatings for EUV lithography [5,6]. This method was recently applied by Stolz et al. to smooth out engineered defects on fused silica substrates onto which  $\text{HfO}_2/\text{SiO}_2$  multilayer coatings were deposited by ion beam sputtering (IBS) [7,8]. This process yielded a 90% reduction in the defect cross-section and 20X increase in the LIDT for high-reflector (HR) coatings at 1064nm and nano-second pulses [8-10].

This  $\text{SiO}_2$  planarization process used upon the substrate was then extended to  $\text{SiO}_2$  planarization of the  $\text{SiO}_2$  layers within a quarter-wave HR stack (termed “multilayer planarization”) designed for 1064nm for planarization of coating defects [10]. Some limitations were discovered for multilayer planarization. In particular, these multilayer planarized coatings showed increased damage density for  $\text{cm}^2$  raster-scanned areas and flat-bottomed interfacial damage craters [10,11]. These damage craters correlated to the top few planarized  $\text{SiO}_2$  layers which suggest that planarized  $\text{SiO}_2$  layers generate a new class of defects. Previous research has discovered planarized  $\text{SiO}_2$  single layers have  $\sim 3\text{x}$  higher absorption at 1064nm than non-planarized (as deposited) control films [12]. While there was no significant impact on the LIDT for single and bilayer coatings damaged with 220ps at 1030nm, the planarized samples experienced higher sloped damage probability curves thus suggesting an increase in the density of defects [12].

Herein the investigation of the planarization process in single SiO<sub>2</sub> layers, HfO<sub>2</sub>/SiO<sub>2</sub> bilayers and, HfO<sub>2</sub>/SiO<sub>2</sub> multilayer high-reflector (HR) coatings and its impact on the laser damage performance when tested at 9ps and 1030nm is reported. The results on these structures show the LIDT is not significantly affected, as found previously in the 220ps pulse duration studies [12]. The planarization process increases the 1064nm absorption of the thin-films which decreases with annealing, thus suggesting the increased absorption is due to oxygen-related defects. Such effects are amplified within high electric-field regions of a HR mirror. The LIDT performance of multilayers at 9ps and 220ps are contrasted. The 9ps LIDT of the multilayer coatings is reduced by ~2x when multilayer planarization is used. Instead, when planarized SiO<sub>2</sub> is used at the substrate-coating interface, a HR stack can be grown with superior LIDT performance. These results suggest the planarization process, which is efficient in smoothing out substrate defects, could be included as a first step in the deposition of multilayer coatings to eliminate the contribution of nodule-like or other imperfections of the substrate to the LIDT.

The sections of the paper are organized as follows. Section 2 describes the experimental methods, including deposition and planarization conditions, coating designs, and their characterization. Section 3 reports the experimental results for each respective coating design. Section 4 analyzes and draws conclusions from the main experimental findings.

## 4.2 EXPERIMENTAL METHODS

### 4.2.1 COATING DESIGNS AND DEPOSITION METHODS

Planarization processing has been discussed in depth elsewhere [9,10]. Generally, this process consists of multiple discrete grow and etch cycles in a 2:1 (deposition : etch) ratio. For this work, ~50nm of SiO<sub>2</sub> was deposited and then ~25nm of the SiO<sub>2</sub> layer was etched. A  $\lambda/4$  SiO<sub>2</sub> (~175nm at  $\lambda=1030$ nm) thickness can be reached in 8 planarization cycles.

Single SiO<sub>2</sub> layers, HfO<sub>2</sub>/SiO<sub>2</sub> bilayers and high reflection HfO<sub>2</sub>/SiO<sub>2</sub> multilayers with and without SiO<sub>2</sub> planarization were investigated. All the coatings were fabricated with a Spector® ion beam

sputtering (IBS) system under conditions which are described in depth elsewhere [12]. The SiO<sub>2</sub> and HfO<sub>2</sub> layers were deposited from a SiO<sub>2</sub> oxide and Hf metallic targets, respectively, with 12sccm oxygen (O<sub>2</sub>) flow directed at the sputtering target for both materials. These coating structures were deposited upon a single batch of UV-grade fused silica 6.35mm thick x 25.4mm diameter cylindrical substrates. The single and bilayer coating designs are summarized in Table 4. Multiple samples were deposited per run to investigate annealing, laser damage, and absorption. Annealing was performed in air at atmospheric pressure at 300°C for soak times of 8hours and 16hours with 1°C/minute rise and fall rates.

Table 4: The coating runs and designs of the samples fabricated for these experiments, where  $L = \lambda/4$  (~175nm) SiO<sub>2</sub> as dep,  $H = \lambda/4$  (~125nm) HfO<sub>2</sub> at  $\lambda = 1030\text{nm}$ , and \* = full  $\lambda/4$  SiO<sub>2</sub> planarized. All SiO<sub>2</sub> layers are  $\lambda/2$  (~350nm) and all HfO<sub>2</sub> layers are  $\lambda/4$  (~125nm).

	Coating 1	Coating 2	Coating 3	Coating 4
<b>As Deposited</b>	[Sub]/[2L]	[Sub]/[2L/H]	[Sub]/[H/2L]	[Sub]/[H]
<b>Planarized</b>	[Sub]/[2L*]	[Sub]/[2L*/H]	[Sub]/[H/2L*]	- - -

The multilayer coatings were  $\lambda/4$  multilayer stacks of HfO<sub>2</sub> and SiO<sub>2</sub> designed for  $\lambda = 1030\text{nm}$  at 0° and are 99.5% reflective. The topmost layer of the multilayer was a  $\lambda/4$  SiO<sub>2</sub> overcoat layer which has been previously shown to increase the LIDT of these coatings [13,14]. Table 5 summarizes the design of the HR stacks and the planarization protocol used in each structure. These structures were annealed following the same process as the thin films detailed above.

Table 5: The coating runs and designs of the samples fabricated for these experiments. Where  $L = \lambda/4$  (~175nm) SiO<sub>2</sub> as dep,  $H = \lambda/4$  (~125nm) HfO<sub>2</sub> at  $\lambda = 1030\text{nm}$ , \* = full  $\lambda/4$  SiO<sub>2</sub> planarized, and \*\* = first half or bottom half of  $\lambda/4$  of SiO<sub>2</sub> planarized.

<b>Planz A</b>	$[\text{Sub}]/[\text{H}/\text{L}^*]^8 / [\text{H}/\text{L}^{**}]^6 / [\text{H}/\text{L}] \text{L}$
<b>Planz B</b>	$[\text{Sub}]/[\text{H}/\text{L}^*]^8 / [\text{H}/\text{L}^{**}]^6 / [\text{H}/\text{L}] \text{L}^*$
<b>Planz C</b>	$[\text{Sub}]/[2\text{L}^*]/[\text{H}/\text{L}]^{15} \text{L}$
<b>Control</b>	$[\text{Sub}]/[\text{H}/\text{L}]^{15} \text{L}$

#### 4.2.2 CHARACTERIZATION METHODS

During planarization processing the SiO<sub>2</sub> material is etched with 1keV argon (Ar) ions accelerated through molybdenum (Mo) grids. Simple Monte Carlo modeling has shown that 1keV Ar<sup>+</sup> have a

penetration depth of  $\sim 3\text{nm}$  [12], thus creating bands of  $\text{SiO}_2$  with potentially higher point defect concentration or impurity implantation. Previous results showed no significant amount of impurity implantation [12]. However, the energetic Ar ions can preferentially sputter oxygen in the growing film, leading to changes in the film's absorption [15,16]. Thus, each of the single and multilayer samples were tested for their absorption loss at  $1\ \mu\text{m}$  wavelength using photothermal common-path interferometry. Each sample was measured in 5-6 spots on the surface with the  $\sim 80\mu\text{m}$  pump beam waist and results averaged.

Assessment of the laser induced damage threshold (LIDT) and damage morphology are critically important features in the behavior of thin films for high-energy laser systems. The LIDT method used for this work was the 1-on-1 shot protocol carried out at  $\lambda = 1030\text{nm}$  with  $\omega_0 = 50\mu\text{m}$  ( $100\mu\text{m}$  beam diameter) at  $e^{-2}$ . ISO: 21254 was followed, except for the spot size requirements. Coating damage was detected through an *in situ* imaging system implemented with 100x long working distance microscope objective. Due to practical requirements, the sample's image was relayed with two lenses before the microscope objective. This damage detection is different from previous measurements [12], in which an *in situ*  $\sim 10\text{x}$  scatter camera and *ex situ* Nomarski microscope at 40x and 100x were used for damage detection. No differences were observed in the LIDT fluence between both detection methods. Nevertheless, LIDT measurements at 220ps on the single and bilayers were repeated for consistency. LIDT measurements were carried out with a Yb:YAG diode pumped CPA laser system with pulse durations of 9ps and 220ps, with and without a laser pulse compressor, respectively [17]. The sample was irradiated at 20 sites per fluence with a spacing of 0.75mm between damage sites. The damage test started at a fluence where all 20 sites damaged – giving a 100% damage probability. The fluence was ramped down, with adequate resolution to define the damage probability curve, until 0 out of 20 irradiated spots were damaged. The LIDT fluence, 50%, and 100% damage probabilities of the coatings were determined with a linear fit of the damage probability curve. The beam diagnostics and fluence

delivered to the sample were assessed from the image of the laser spot at the sample obtained with an Andor iKon-M CCD camera cooled to  $-20^{\circ}\text{C}$ . The image intensity distribution was fitted to a Gaussian. The integrated counts were linearly related to the pulse energy through the energy calibration and the beam diameter calculated from the fit. The fluence was then calculated using ISO: 21254.

### 4.3 RESULTS

#### 4.3.1 SINGLE AND BILAYER LASER DAMAGE

Summarized below are the results of the as as-deposited and planarized  $\text{SiO}_2$  single layers and  $\text{SiO}_2/\text{HfO}_2$  bilayers obtained from the analysis of the 9ps laser damage tests. Figure 28 shows the damage probability diagrams of coating 1 as-deposited and planarized. The results show there is a  $\sim 20\%$  increase in the LIDT for planarized single layer  $\text{SiO}_2$  coatings. This is in contradiction to the 220ps results for the same coating design and the other planarized coatings previously reported [12].

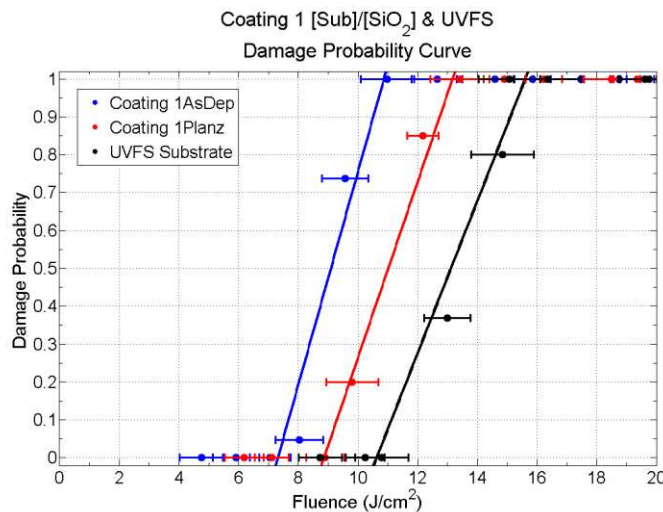


Figure 28: The damage probability diagram at 9ps pulse duration for coating 1 (as-deposited and planarized) and UV-grade fused silica substrate.

The morphology of the damage in coating 1 was evaluated from the Nomarski images shown in Figure 29, and compared to that of the fused silica substrates. It consists of high density pitting with each pit being  $5 - 10\mu\text{m}$  in diameter.

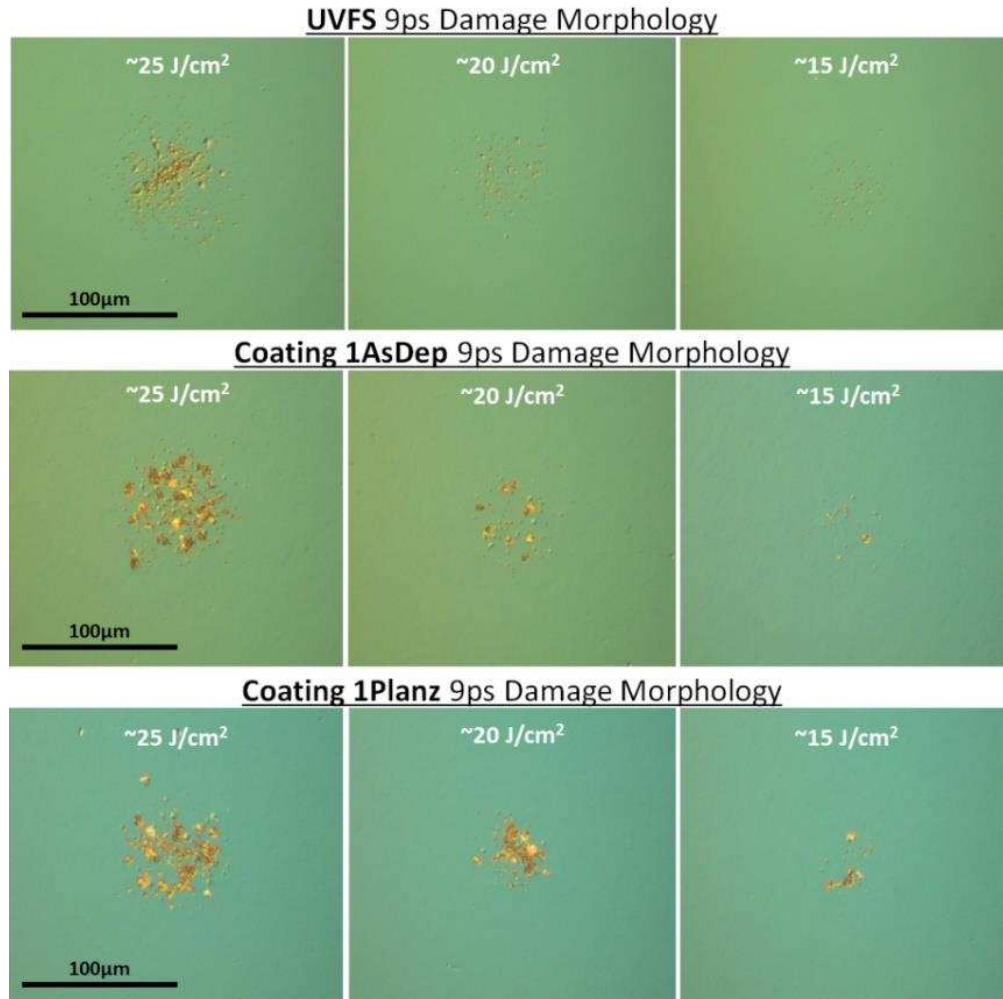


Figure 29: The damage morphology for laser damage at 9ps for high, mid, and low fluence for UV-grade fused silica substrate and 1AsDep and 1Planz.

Laser damage probability curves for coatings 2, 3 and 4 are displayed in Figure 30A and 30B. Coating 2 attempts to replicate the bottom two layers near the substrate of a high-reflector multilayer coating. While coating 3 replicates the top two layers of a high reflector. In contrast to the behavior of coating 1, the as-deposited samples have a higher LIDT than the corresponding coating with planarized SiO<sub>2</sub>.

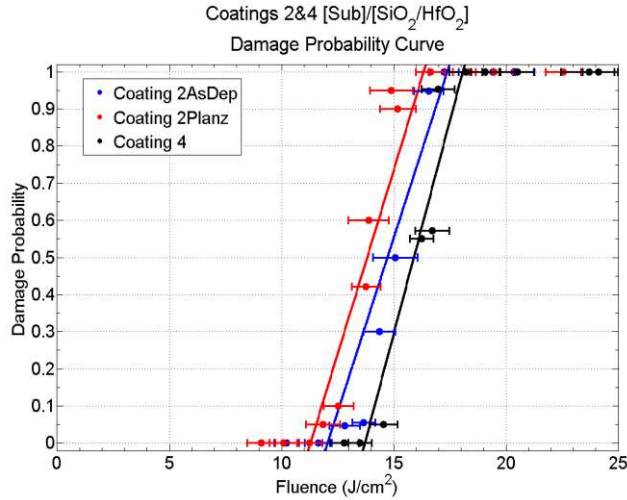


Figure 30A: The damage probability versus fluence at 9ps pulse duration for coating 2 (as deposited and planarized) and coating 4.

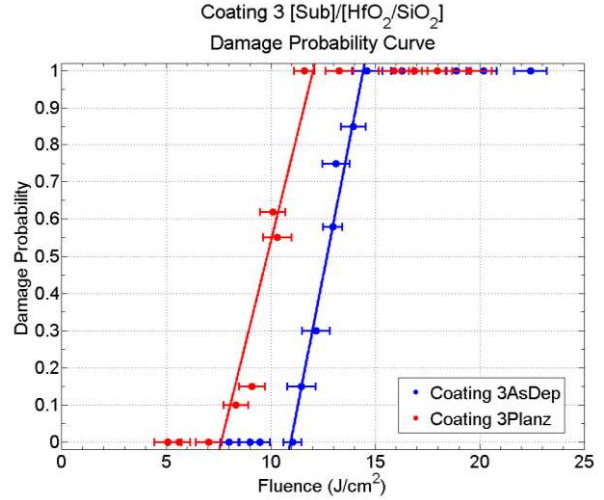


Figure 30B: The damage probability diagram at 9ps pulse duration for coating 3 as deposited and planarized.

To compare the LIDT fluence values across the set of coatings the standing wave electric field within the coatings is evaluated and shown in Figure 31. The LIDT of single, bilayers, and anti-reflection coatings tends to be mediated by the substrate-coating interface [20-22]. For this reason, the LIDT values for coatings 2, 3, and 4 were normalized by  $(E_i^2/E_1^2)$  where  $i=2,3,4$  and  $E_1^2$  is the electric field intensity at the substrate-coating interface of coating 1. The normalized LIDT and absorption loss are summarized in Table 6.

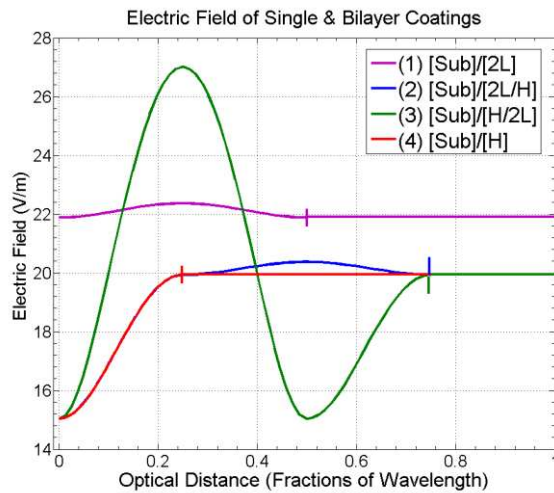


Figure 31: Calculated electric field within the single and bilayer coatings for  $\lambda=1030\text{nm}$  and normal

incidence. The air-film interface is labeled as zero optical distance ( $y$ -axis intercept). The vertical tick marks indicate the coating-substrate interface for each respective coating design.

Table 6: Normalized LIDT for all single and bilayer coatings measured at 9ps and 220ps. The 220ps LIDT data are averaged between the present and previous measurements [12].

Sample	LIDT ( $J/cm^2$ )		Absorption (ppm)
	$\tau = 9ps$	$\tau = 220ps$	
UVFS	<b>11.2 <math>\pm</math> .6</b>	<b>36.8 <math>\pm</math> .8</b>	< 1.0
Coating 1AsDep	<b>6.9 <math>\pm</math> .6</b>	<b>13.0 <math>\pm</math> .7</b>	5.4 $\pm$ 0.2
Coating 1Planz	<b>8.6 <math>\pm</math> .7</b>	<b>11.4 <math>\pm</math> .8</b>	15.0 $\pm$ 0.3
Coating 2AsDep	<b>10.0 <math>\pm</math> .6</b>	<b>14.9 <math>\pm</math> .7</b>	13.5 $\pm$ 0.9
Coating 2Planz	<b>9.3 <math>\pm</math> .6</b>	<b>15.2 <math>\pm</math> .7</b>	23.2 $\pm$ 0.6
Coating 4	<b>11.3 <math>\pm</math> .6</b>	<b>16.4 <math>\pm</math> .6</b>	6.4 $\pm$ 0.3
Coating 3AsDep	<b>9.1 <math>\pm</math> .4</b>	<b>10.2 <math>\pm</math> .5</b>	10.1 $\pm$ 0.4
Coating 3Planz	<b>6.3 <math>\pm</math> .4</b>	<b>7.4 <math>\pm</math> .4</b>	19.2 $\pm$ 0.2

The results of Table 3 show there is a consistent increase in the absorption loss when the  $SiO_2$  layer is planarized. Previous results [12] showed a similar behavior. This increase is ascribed to the generation of oxygen defects due to the preferential sputtering of oxygen by the 1 keV Ar ions.

Table 3 also compares the normalized LIDT of the different coating structures obtained when testing with 9ps and 220ps pulse duration. Two important observations are drawn from these data: a) the scaling of LIDT with pulse duration ( $\tau$ ) is lower than the  $\tau^{0.5}$  observed in the UVFS substrate; b) there is a correlation between LIDT and absorption loss at 9ps and 220ps for single layers, except for coating 1.

Annealing is known to reduce absorption losses, in part due to the reduction of oxygen defects, such as dangling bonds, vacancies, or interstitials [23]. This is observed in all coatings, with the largest change in the absorption loss observed in the planarized samples. As shown in Figure 32, 8 hours of soaking at 300°C is sufficient to reduce losses to <5ppm.

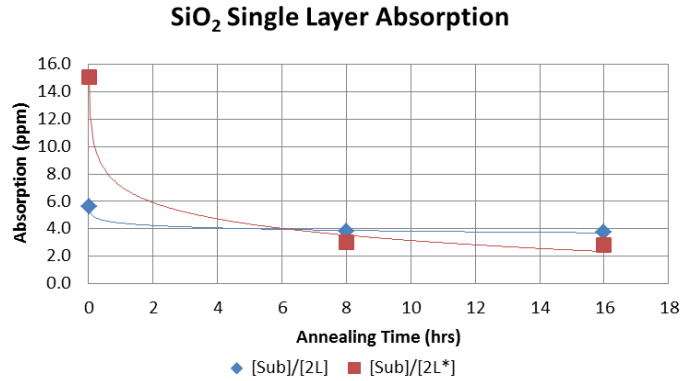


Figure 32: The dependence on absorption with annealing time for coating 1 design (SiO<sub>2</sub> single layer).

These annealed coatings were laser damage tested. The results are summarized in Table 7 below.

Generally, annealing increased the LIDT to varying degrees for both 9ps and 220ps pulse duration.

Table 7: Coating-substrate interface E<sup>2</sup> normalized LIDT and absorption data for annealed coatings.

Laser Damage and Absorption of Post-Annealed Coatings			
Sample	LIDT (J/cm <sup>2</sup> )		Absorption (ppm)
	$\tau = 9\text{ps}$	$\tau = 220\text{ps}$	
Coating 1AsDep (300C 8hr)	<b>8.8 ± .5</b>	<b>14.1 ± .7</b>	3.83 ± 0.2
Percent Change (w/ Annealing)	28%	1%	-29%
Coating 1Planz (300C 8hr)	<b>12.1 ± .7</b>	<b>20.4 ± .7</b>	3.0 ± 0.3
Percent Change (w/ Annealing)	41%	79%	-80%
Coating 2AsDep	<b>12.8 ± .7</b>	<b>16.5 ± .7</b>	3.7 ± 0.9
Percent Change (w/ Annealing)	28%	10%	-72%
Coating 2Planz	<b>11.9 ± .6</b>	<b>16.6 ± .7</b>	5.1 ± 0.6
Percent Change (w/ Annealing)	27%	9%	-78%
Coating 4	<b>11.6 ± .6</b>	---	1.7 ± 0.3
Percent Change (w/ Annealing)	2%	---	-73%
Coating 3AsDep	<b>10.1 ± .6</b>	<b>10.9 ± .6</b>	4.1 ± 0.3
Percent Change (w/ Annealing)	11%	7%	-60%
Coating 3Planz	<b>7.8 ± .5</b>	<b>10.8 ± .6</b>	3.9 ± 0.2
Percent Change (w/ Annealing)	24%	47%	-80%

### 4.3.2 MULTILAYER LASER DAMAGE

The damage probability curves for the HR coatings deposited with different SiO<sub>2</sub> planarization strategies (Table 5) and corresponding damage morphologies are shown in Figure 33 and Figure 34 for 9ps and 220ps pulse durations, respectively. These results along with values of the absorption loss at 1064nm are compiled in Table 8.

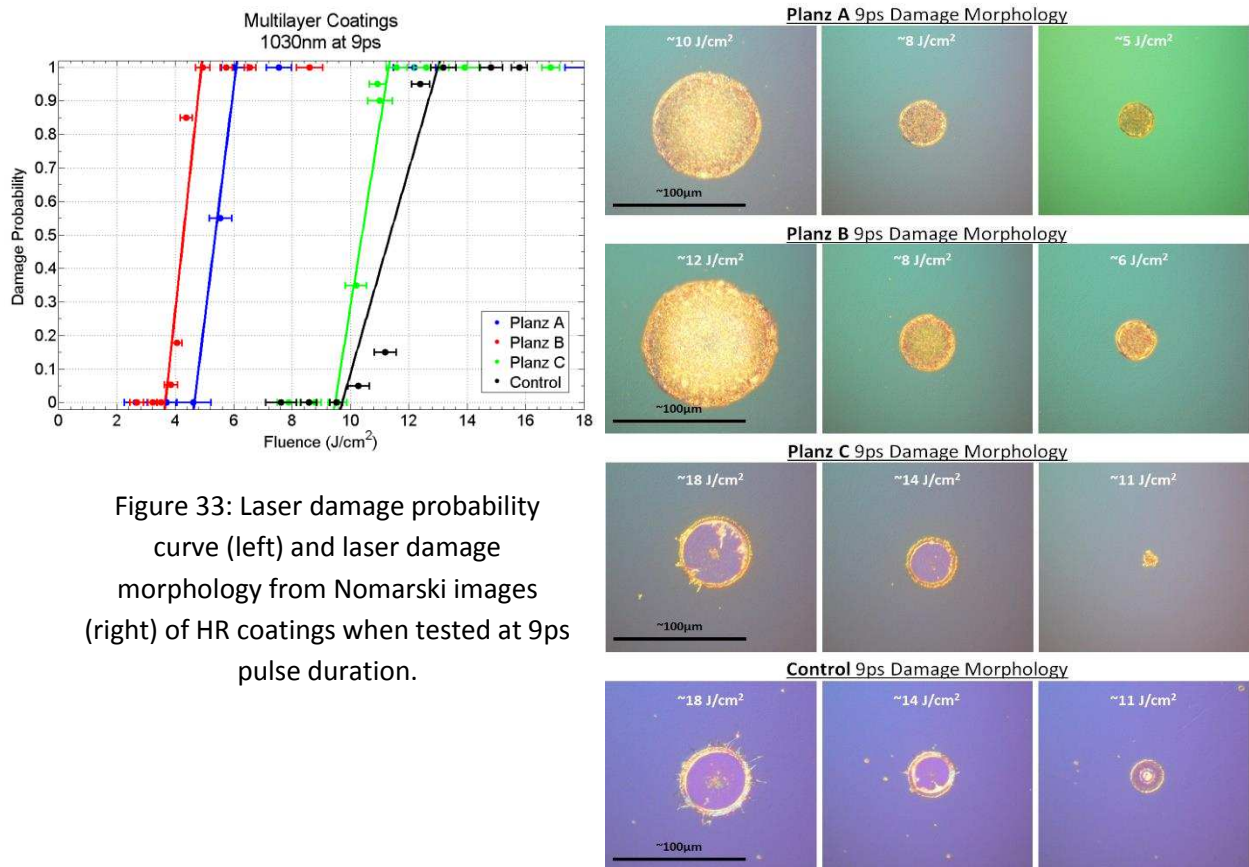


Figure 33: Laser damage probability curve (left) and laser damage morphology from Nomarski images (right) of HR coatings when tested at 9ps pulse duration.

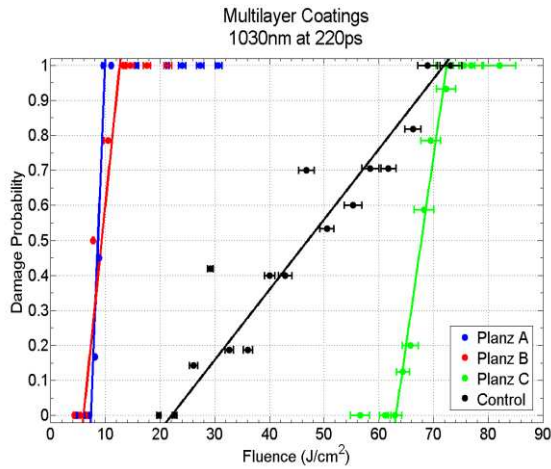


Figure 34. Laser damage probability curve (left) and laser damage morphology (right) from Nomarski images of HR coatings when tested at 220ps pulse.

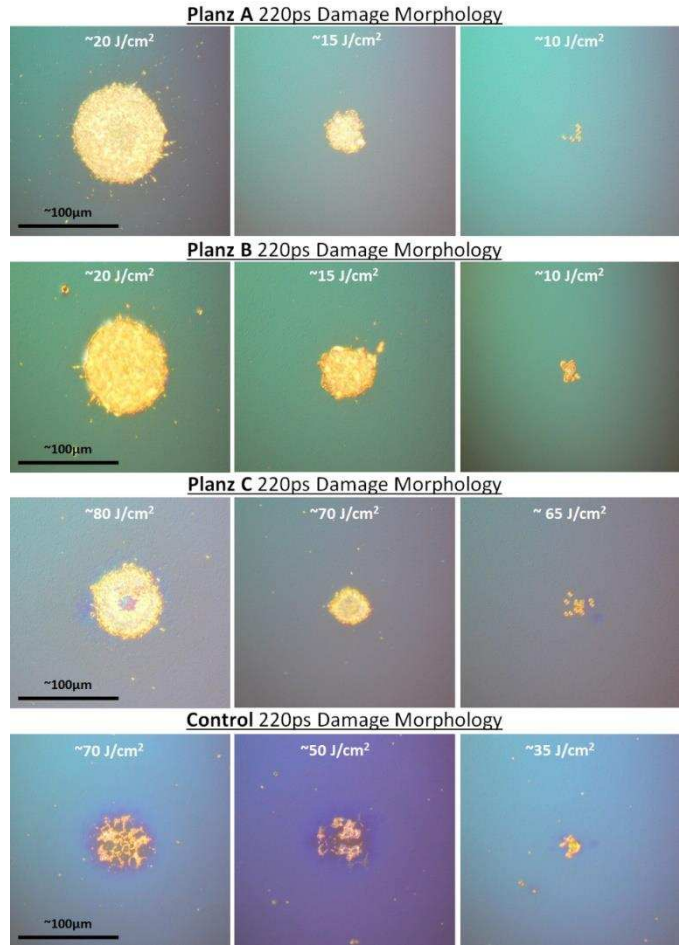


Table 8: Laser damage fluence and absorption loss for the multilayer coatings

Sample	Laser Damage ( $J/cm^2$ ) $\tau = 9 \text{ ps}$			Laser Damage ( $J/cm^2$ ) $\tau = 220 \text{ ps}$			Absorption loss @1064 nm
	LIDT	50%	100%	LIDT	50%	100%	
	Planz A	$4.7 \pm .3$	5.4	6.1	$6.8 \pm .3$	8.6	
Planz B	$3.7 \pm .3$	4.3	4.9	$6.3 \pm .3$	8.8	11.2	175 ppm
Planz C	$9.5 \pm .3$	10.4	11.3	$63.1 \pm 1.2$	67.8	72.4	40 ppm
Control	$9.7 \pm .3$	11.4	13.2	$21.5 \pm .5$	46.0	70.5	35 ppm

The most striking behavior that can be extracted from these results is that multilayer planarization drastically reduces the LIDT when tested at 9ps and 220ps. The large values of the absorption loss at 1064 nm are indicative of a deterioration of the optical quality of the multilayer in the fully planarized HR multilayer structures. The steep slope of the probability curves with fluence suggests that a single type of defect dominates in the laser damage behavior at both pulse durations. Instead, the

control sample at 220ps has low slope suggesting a different family of defects at lower density are responsible for the damage initiation. The damage morphology at 9ps and 220ps of Planz A and Planz B coatings indicates melting which is likely induced by the high density of absorbers at 1 $\mu$ m wavelength.

Annealing of the multilayers is shown in Figure 35. The largest variations in the absorption loss with annealing are observed in the Planz A and Planz B coatings. Instead the Control and Planz C coating show a 75% and 85% in absorption to  $\sim$ 10ppm and  $\sim$ 5ppm, respectively.

The impact of annealing with LIDT on the HRs is summarized in Table 9. Annealing increases LIDT at 220ps of the planarized samples, except in the case of Planz C. This is because the planarized layer is located in a region of the coating where the amplitude of the standing wave electric field is small compared to that at the air-coating interface. The recovery of the LIDT of the control sample to values that approach the LIDT of Planz C with annealing is an indication that the structural quality of this sample may have been altered during the deposition process. On the assumption that annealing reduces oxygen defect concentration, the results show that this type of defects have a minor contribution to laser damage initiation at 9ps pulse duration.

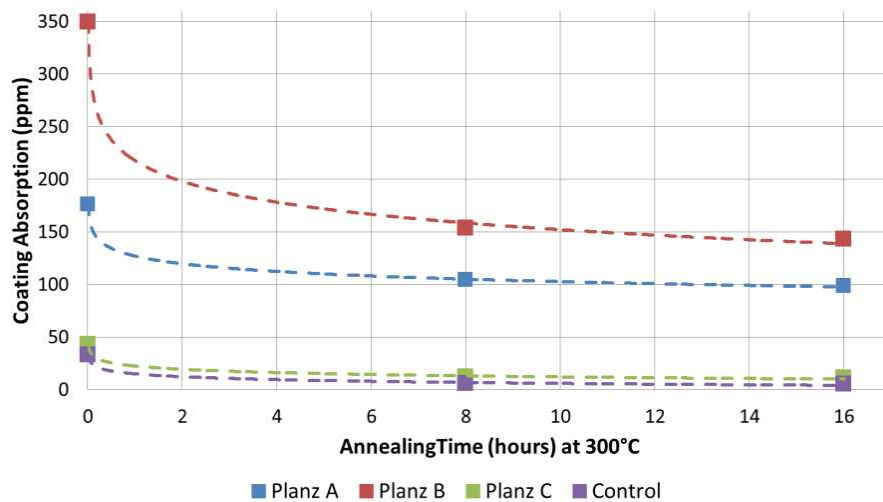


Figure 35: Multilayer coating absorption for various annealing times. Uncertainties are too small to report in the plot.

Table 9: The LIDT, 50%, and 100% damage probability at 9ps and 220ps for annealed HR coatings. Also reported is the percent change with annealing as compared to the non-annealed.

Sample Notes	Laser Damage (J/cm <sup>2</sup> )					
	$\tau = 220\text{ps}$			$\tau = 9\text{ps}$		
	LIDT	50%	100%	LIDT	50%	100%
<b>Planz A : [Sub][H/L*]<sup>8</sup>[H/L**]<sup>6</sup>[H/L]L</b>						
Planz A (300°C 16hr)	<b>14.3 ± .3</b>	15.5	16.7	<b>5.2 ± .3</b>	6.0	6.8
Percent Change	111%	81%	61%	11%	11%	12%
<b>Planz B : [Sub][H/L*]<sup>8</sup>[H/L**]<sup>6</sup>[H/L]L*</b>						
Planz B (300°C 16hr)	<b>16.0 ± .3</b>	18.7	21.4	<b>4.0 ± .3</b>	4.3	4.5
Percent Change	153%	113%	90%	11%	0%	-9%
<b>Planz C : [Sub][2L*][H/L]<sup>15</sup>L</b>						
Planz C (300°C 16hr)	<b>66.9 ± 1.2</b>	71.7	76.5	<b>10.5 ± .3</b>	11.1	11.6
Percent Change	6%	6%	6%	11%	6%	2%
<b>Control : [Sub][H/L]<sup>15</sup>L</b>						
Control (300°C 16hr)	<b>46.4 ± .5</b>	63.7	80.9	<b>11.3 ± .3</b>	12.3	13.3
Percent Change	116%	38%	15%	16%	7%	1%

#### 4.4 DISCUSSION AND CONCLUSION

Thin-films deposited by IBS can contain coating flake defects and/or nanometric absorbing defects inherent to the deposition process. These defects play a role in the laser damage resistance. In this study of SiO<sub>2</sub> planarization, the results suggest the process contributes to increase the density of these nanometric absorbing defects, through the preferential sputtering of oxygen by the energetic Ar ions used for planarization. These defects can be recovered by annealing the coatings at 300°C for over 8 hours, as evidenced by the decrease in absorption in single layers, bilayers, and multilayers.

In general, the LID morphology is analogous to the recent observation by S. Ly *et al.* [19] for laser damage at 1053nm with 1 – 60ps pulse duration. This morphology is also characteristics of damage in coatings 2, 3 and 4. In contrast, the damage morphology of the UVFS at 220ps showed circular damage craters, similar to the results of S. Ly *et al.* for long pulses [12,18,19].

Nanometric defects can affect the LIDT. Different studies have investigated their size dependent [26], and distribution within the bulk or interfaces [27-29] in affecting LIDT, and others have investigated

their role in LIDT at different pulse durations [1,18,19,21]. The results described above are consistent with these previous findings. They show that in the case of strong absorption – large density of nanometric defects – as is the case in the HR coatings the LIDT reduces, when tested at 9ps and 220ps. Annealing out these defects improves the 220ps LIDT to a greater extent as compared to the 9ps LIDT results. The morphology of the damage sites of the HR coatings with very high absorption is indicative of the dominance of thermal processes affecting laser damage initiation.

While the planarization process mainly increases nanometric defects on the SiO<sub>2</sub> layers, if such layer is introduced in regions of a multilayer where the standing wave electric field is low (i.e. the substrate-coating interface) the LIDT of a high-quality HR is not impacted. As such, a planarized sacrificial layer introduced between the substrate and the coating could be used to remove any influence of the substrate in affecting the structural, optical and damage behavior of multilayer dielectric coatings.

## REFERENCES

1. Wood, Roger M. Laser-induced damage of optical materials. CRC Press, 2003.
2. Guenther, Karl H. "Nodular defects in dielectric multilayers and thick single layers." *Applied optics* 20.6 (1981): 1034-1038.
3. Kozlowski, Mark R., et al. *Influence of defect shape on laser-induced damage in multilayer coatings*. No. UCRL-JC--115161; CONF-9406168--2. Lawrence Livermore National Lab., CA (United States), 1994.
4. Stolz, Christopher J., et al. *A comparison of nodular defect seed geometries from different deposition techniques*. No. UCRL-JC--121628; CONF-9510106--3. Lawrence Livermore National Lab., CA (United States), 1995.
5. Mirkarimi, Paul B., et al. "Advancing the ion beam thin film planarization process to mitigate EUVL mask substrate pit defects." 2004 EUVL Symposium. 2004.
6. Mirkarimi, P. B., et al. "Advancing the ion beam thin film planarization process for the smoothing of substrate particles." *Microelectronic engineering* 77.3 (2005): 369-381.
7. Stolz, Christopher J., et al. "Planarization of optical substrates." U.S. Patent Application No. 14/434,699.
8. Stolz, Christopher J., et al. "High laser-resistant multilayer mirrors by nodular defect planarization [Invited]." *Applied optics* 53.4 (2014): A291-A296.
9. Stolz, Christopher J., et al. "Defect insensitive 100 J/cm<sup>2</sup> multilayer mirror coating process." SPIE Laser Damage. International Society for Optics and Photonics, 2013.
10. Stolz, Christopher J., et al. "Substrate and coating defect planarization strategies for high-laser-fluence multilayer mirrors." *Thin Solid Films* 592 (2015): 216-220.
11. Stolz, Christopher J., et al. "Depth determination of critical fluence-limiting defects within planarized and non-planarized mirror coatings." SPIE Optical Systems Design. International Society for Optics and Photonics, 2015.
12. Day, T., et al. *Impacts of SiO<sub>2</sub> planarization on optical thin film properties and laser damage resistance*. No. LLNL-PROC-713180. Lawrence Livermore National Laboratory (LLNL), Livermore, CA, 2016.
13. Schiltz, D., et al. "Modification of multilayer mirror top-layer design for increased laser damage resistance." *SPIE Laser Damage*. International Society for Optics and Photonics, 2014.
14. Stolz, Christopher J., et al. *Effect of SiO<sub>2</sub> overcoat thickness on laser damage morphology of HfO<sub>2</sub>/SiO<sub>2</sub> Brewsters angle polarizers at 1064 nm*. No. UCRL-JC--124875; CONF-961070--15. Lawrence Livermore National Lab., CA (United States), 1997.
15. Patel, D., et al. "SiO<sub>2</sub>/HfO<sub>2</sub> multilayers: impact of process parameters and stack geometry on the optical and structural properties." *Proc. SPIE*. Vol. 7132. 2008.
16. Langdon, B., et al. "Influence of process conditions on the optical properties HfO<sub>2</sub>/SiO<sub>2</sub> thin films for high power laser coatings." *Proc. SPIE*. Vol. 6720. 2007.
17. Baumgarten, Cory, et al. "1 J, 0.5 kHz repetition rate picosecond laser." *Optics Letters* 41.14 (2016): 3339-3342.
18. Ly, S., et al. "The role of defects in laser-induced modifications of silica coatings and fused silica using picosecond pulses at 1053 nm: I. Damage morphology." *Optics Express* 25.13 (2017): 15161-15178.
19. Laurence, T. A., et al. "Role of defects in laser-induced modifications of silica coatings and fused silica using picosecond pulses at 1053 nm: II. Scaling laws and the density of precursors." *Optics Express* 25.13 (2017): 15381-15401.

20. Papernov, Semyon, et al. "One step closer to the intrinsic laser damage threshold of HfO<sub>2</sub> and SiO<sub>2</sub> monolayer thin films." *Laser-Induced Damage in Optical Materials: 1997*. International Society for Optics and Photonics, 1998.
21. Smith, Arlee V., and Binh T. Do. "Bulk and surface laser damage of silica by picosecond and nanosecond pulses at 1064 nm." *Applied optics* 47.26 (2008): 4812-4832.
22. Apfel, J. H., et al. *Effects of barrier layers and surface smoothness on 150-ps, 1.064- $\mu$ m laser damage of AR coatings on glass*. No. UCRL-80043; CONF-771061-3. Optical Coating Lab., Inc., Santa Rosa, Calif.(USA); California Univ., Livermore (USA). Lawrence Livermore Lab., 1977.
23. Polenzky, Christina, Christoph Rickers, and Michael Vergöhl. "Properties of cosputtered SiO<sub>2</sub>-Ta<sub>2</sub>O<sub>5</sub>-mixtures." *Thin Solid Films* 517.10 (2009): 3126-3129.
24. Griscom, David L. "Optical properties and structure of defects in silica glass." *Journal of the Ceramic Society of Japan* 99.1154 (1991): 923-942.
25. Devine, R. A. B., and A. Golanski. "Creation and annealing kinetics of magnetic oxygen vacancy centers in SiO<sub>2</sub>." *Journal of Applied Physics* 54.7 (1983): 3833-3838.
26. Gallais, Laurent, et al. "Investigation of nanodefekt properties in optical coatings by coupling measured and simulated laser damage statistics." *Journal of Applied Physics* 104.5 (2008): 053120.
27. Krol, Helene, et al. "Investigation of nanoprecursors threshold distribution in laser-damage testing." *Optics Communications* 256.1 (2005): 184-189.
28. Papernov, S., and A. W. Schmid. "Using gold nanoparticles as artificial defects in thin films: what have we learned about laser-induced damage driven by localized absorbers?" *Proc. SPIE*. Vol. 6403. 2007.
29. Yu, Zhenkun, et al. "Damage threshold influenced by the high absorption defect at the film–substrate interface under ultraviolet laser irradiation." *Optics letters* 38.21 (2013): 4308-4311.

## CHAPTER 5

### CONCLUSION AND FUTURE WORK

This thesis combines work on SiO<sub>2</sub> planarization in single SiO<sub>2</sub> layers, SiO<sub>2</sub>/HfO<sub>2</sub> bilayer, and multilayer coatings for use in high-energy laser systems. The optical absorption loss, impurity implantation, laser damage resistance at 220ps and 9ps, laser damage morphology, and annealing properties were investigated.

A 2-3x increase in absorption loss from control to planarized coatings was found. Little evidence of impurities was found with XPS and SEM-EDS. Additionally, the absorption loss of the single and bilayer coatings decreases (for both planarized and as deposited) with post-process annealing, which signifies the absorption is caused by oxygen related defects. These defects are attributed to the preferential sputtering of oxygen during planarization out of the SiO<sub>2</sub> material and the production of oxygen-deficiency centers. Laser damage studies on single SiO<sub>2</sub> and HfO<sub>2</sub>/SiO<sub>2</sub> bilayer coatings at 220ps found insignificant changes (<10%) in the LIDT between control and planarized coatings. However, the laser damage probability curves of the planarized coatings had higher slopes. This, along with the increased absorption, suggests a larger density of point-defects which contribute to laser damage. For the single SiO<sub>2</sub> layer damage at 9ps, the planarized sample had slightly higher ( For the same single and bilayer coatings damaged at 9ps, the LIDT also shows <15% decrease between control and planarized coatings. It is known that the laser damage properties of single, bilayer, and AR coatings are mediated by the substrate-coating interface. It is possible extrinsic mechanisms mask the effects of planarization, thus future work should be dedicated to uncovering this process. Comparing between pulse durations, the UV-grade fused silica substrate follows the LIDT pulse duration scaling ( $\tau^{0.5}$ ) yet the coatings do not. In fact, some coating LIDT are nearly equal at 9ps and 220ps. This further signifies that extrinsic mechanisms contribute to the laser damage.

The multilayer planarization coatings show large absorption losses, particularly for the design with SiO<sub>2</sub> planarization within the high electric-field areas. With post-annealing, the absorption decreases exponentially for all coatings. Laser damage of multilayer coatings at 220ps shows large differences in LIDT with planarization design. The multilayer planarized coatings (Planz A and Planz B) show low LIDT and sharp slopes, which indicates the planarization induced absorption dominates the laser damage. Planz C coatings shows remarkably high LIDT and sharp laser damage probability slope at 220ps, signifying an intrinsic laser damage mechanism. However, the Control coating showed a relatively low LIDT and low laser damage probability slope, thus signifying a different family of large-scale defects at lower density contribute to the laser damage. In reality, the Control coating's LID characteristics are anomalous and not indicative of a typical high-quality IBS coating. Further research should be dedicated to creating high quality coating without coating defects. When damaged at 9ps, the coatings also show a dependence on multilayer planarization and absorption, however to a lesser degree than 220ps. Interestingly, the Planz C and Control coatings, whom had largely different LIDT at 220ps, have equal LIDT at 9ps. It is likely, and supported by literature, that the low-density coating defects within the Control coating do not play a role at 9ps, thus equalizing the LIDT. Further research should be dedicated to comparing the different defect types which contribute to laser damage within the long and short pulse regime.

The future work in laser induced damage of single and bilayer coatings should be dedicated to extracting the combinatory effects of damage originating within the coating and damage originating at the substrate-coating interface. These extrinsic effects are partially responsible for laser damage initiation and thus muddle the differences between the planarized and as deposited coatings. Additionally, further research should be conducted to reveal the true nature of the point defects implanted into the planarized SiO<sub>2</sub>. At what energy within the band gap does the oxygen vacancy defect lie? How does this defect contribute to laser induced damage at ultra-short (<1ps) pulse widths and

shorter wavelengths? Furthermore, for planarized multilayer coatings employing planarization at the substrate-coating interface gives the beneficial combination of mitigating nodular defects without increasing the absorption and reducing the laser damage resistance. Additional engineering approaches should also be investigated in future work.